nature materials

ARTICLES

PUBLISHED ONLINE: 16 OCTOBER 2017 | DOI: 10.1038/NMAT5005

Sequential bottom-up assembly of mechanically stabilized synthetic cells by microfluidics

Marian Weiss[1,2†], Johannes Patrick Frohnmayer[1,2†], Lucia Theresa Benk[1,2†], Barbara Haller[1,2], Jan-Willi Janiesch[1,2], Thomas Heitkamp[3], Michael Börsch[3], Rafael B. Lira[4], Rumiana Dimova[4], Reinhard Lipowsky[4], Eberhard Bodenschatz[5], Jean-Christophe Baret[6,7], Tanja Vidakovic-Koch[8], Kai Sundmacher[8,9], Ilia Platzman[1,2*] and Joachim P. Spatz[1,2*]

Compartments for the spatially and temporally controlled assembly of biological processes are essential towards cellular life. Synthetic mimics of cellular compartments based on lipid-based protocells lack the mechanical and chemical stability to allow their manipulation into a complex and fully functional synthetic cell. Here, we present a high-throughput microfluidic method to generate stable, defined sized liposomes termed 'droplet-stabilized giant unilamellar vesicles (dsGUVs)'. The enhanced stability of dsGUVs enables the sequential loading of these compartments with biomolecules, namely purified transmembrane and cytoskeleton proteins by microfluidic pico-injection technology. This constitutes an experimental demonstration of a successful bottom-up assembly of a compartment with contents that would not self-assemble to full functionality when simply mixed together. Following assembly, the stabilizing oil phase and droplet shells are removed to release functional self-supporting protocells to an aqueous phase, enabling them to interact with physiologically relevant matrices.

The formation of lipid membrane-based compartments is one of the distinguishing features of eukaryotic cells. Compartments provide physical and chemical barriers that prevent the uncontrolled diffusion of molecular components to and from the surrounding environment, thereby allowing independent and self-contained metabolic, signalling, or synthesizing activities[1–4]. Moreover, biological membranes allow for chemically selective intra- and intercellular material transport and signal transduction by various transmembrane proteins, such as ion channels and receptors[5,6]. In the context of synthetic biology, protocells are synthetic, biomolecule-containing, lipid-based compartments. These compartments can either be small, large or giant unilamellar vesicles (SUVs, LUVs or GUVs)[7,8]. The chemical and mechanical instabilities of phospholipids under high ionic strength conditions, especially multivalent cations, and their sensitivity to pH changes are considered to be the main challenges in utilizing protocells for synthetic biology[9–11]. In addition, inserting molecules into protocells represents a particular challenge given their impermeability and mechanical instability[12].

Polymersomes made from amphiphilic block copolymers constitute alternative compartments to protocells. They enclose and are surrounded by an aqueous solution[13]. Some polymersomes can be engineered with transmembrane proteins or synthetic channel molecules that enable certain chemicals to pass the polymer membrane[14,15]. They are both chemically and mechanically more stable than protocells and are adjustable to certain environments and functionalities[13]. In contrast to GUVs, where the manipulation of chemical and physical properties bears limitations, the thickness, bending and stretching moduli of the polymeric membrane is tuned by changing the block-copolymer molecular properties. However, the encapsulation of biomolecules and further manipulation of traditional water-in-water polymersomes still represent challenges. The uncontrolled permeability of the polymersomes[16,17] and a lack of technologies which allow for the precise and efficient delivery of different biological components are the main drawbacks.

In contrast to polymersomes, copolymer-stabilized water-in-oil droplet compartments can be manipulated at high throughput using automated microfluidic technologies[18,19]. The biophysical properties of droplet-based compartments, their ultra-fast generation (up to 1 MHz), and the high degree to which this micro-environment is controllable add up to a system that combines the necessary requirements of various synthetic biology applications[20–22]. Moreover, it was shown that the continuous oil phase and its additives play an important role not only in the stable separation of the droplets and in preserving the bio-content[23] but also in the combinatorial delivery of biological materials exclusively into the droplets by means of microfluidic pico-injection technology[24]. However, much like in the case of polymersomes, the ability of the droplets to serve as optimal cell-like compartments is mainly hindered by their inability to imitate the biophysical properties of cellular lipid membranes[17,25].

[1]Department of Cellular Biophysics, Max Planck Institute for Medical Research, Jahnstraße 29, 69120 Heidelberg, Germany. [2]Department of Biophysical Chemistry, University of Heidelberg, Im Neuenheimer Feld 253, 69120 Heidelberg, Germany. [3]Single-Molecule Microscopy Group, Jena University Hospital, Friedrich Schiller University Jena, 07743 Jena, Germany. [4]Theory & Bio-Systems, Max Planck Institute of Colloids and Interfaces, 14424 Potsdam, Germany. [5]Laboratory for Fluid Dynamics, Pattern Formation and Biocomplexity, Max Planck Institute for Dynamics and Self-Organization, 37077 Göttingen, Germany. [6]Droplets, Membranes and Interfaces, Max Planck Institute for Dynamics and Self-Organization, 37077 Göttingen, Germany. [7]Soft Micro Systems, CNRS, Univ. Bordeaux, CRPP, UPR 8641, 115 Avenue Schweitzer, 33600 Pessac, France. [8]Process System Engineering, Max Planck Institute for Dynamics of Complex Technical Systems, 39106 Magdeburg, Germany. [9]Otto-von-Guericke University Magdeburg, Process Systems Engineering, Universitätsplatz 2, 39106 Magdeburg, Germany. [†]These authors contributed equally to this work. *e-mail: ilia.platzman@mpimf-heidelberg.mpg.de; joachim.spatz@mpimf-heidelberg.mpg.de

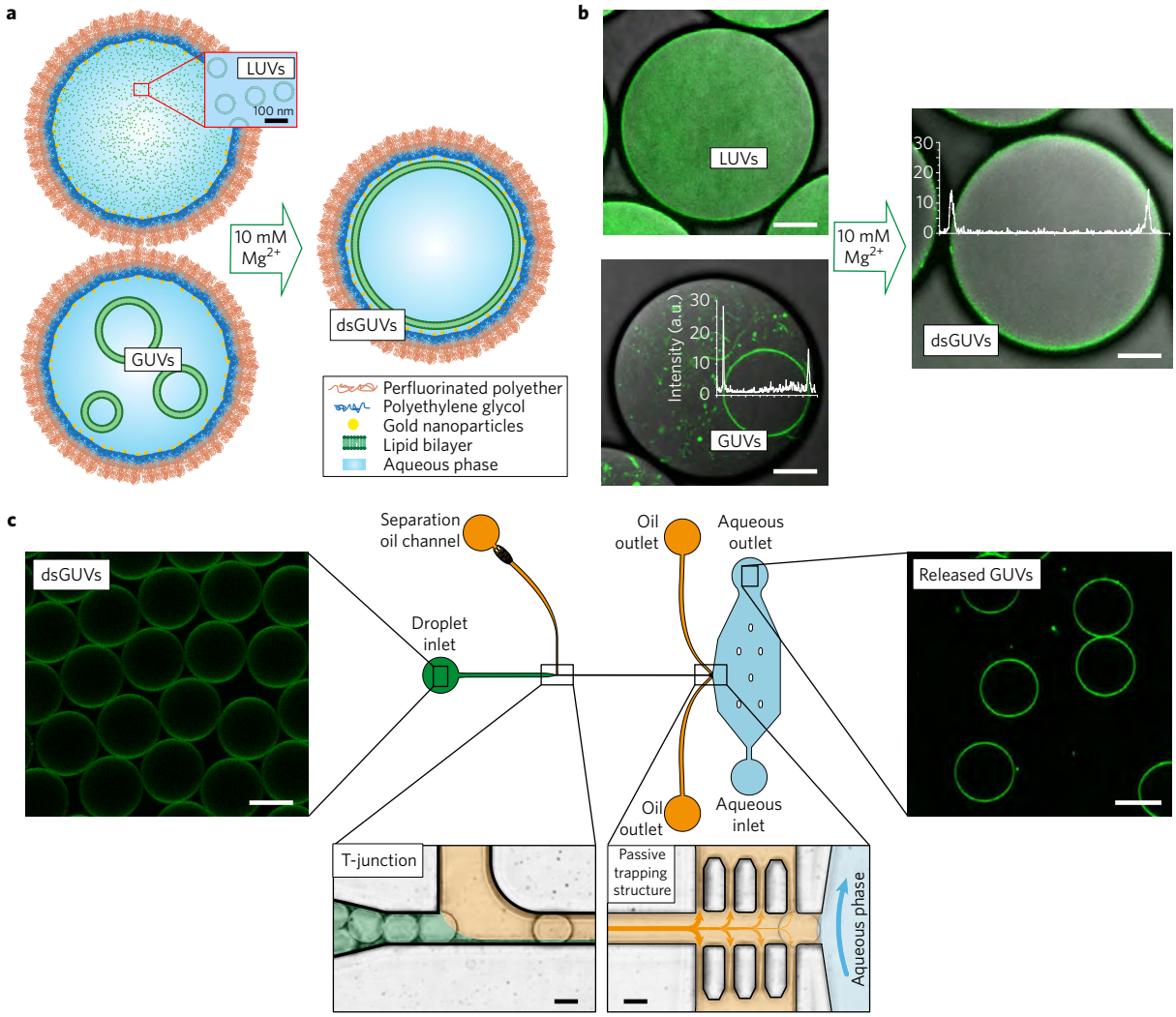

Figure 1 | Formation and analysis of droplet-stabilized GUVs. a, Lipid vesicles, either LUVs or GUVs, were encapsulated in water-in-oil copolymer-stabilized droplets by means of microfluidics. To transform the encapsulated vesicles into a supported lipid bilayer at the copolymer-stabilized droplets' inner interface, 10 mM Mg^{2+} was applied during droplet production or by means of pico-injection. **b**, Representative combined images of green fluorescence from lipids (ATTO 488-labelled DOPE) and bright-field microscopy of the encapsulated LUVs and GUVs, and of the dsGUVs. The latter two images show superimposed the fluorescence intensity profile. Scale bar, 10 μm. **c**, The microfluidic device designed to release the assembled lipid compartments from the surrounding stabilizing polymer droplets into the aqueous phase. The left image shows the fluorescence images of the monodisperse dsGUVs in the oil phase prior to release. After injection, droplets are separated from each other at a T-junction where a tributary oil flow containing 20 vol% destabilizing surfactants merges with the droplet flow. Passive trapping structures within the microfluidic channel enable the draining of the continuous oil phase into adjacent oil outlets and decelerate the droplets before they enter the aqueous phase. A comparison of dsGUVs and released lipid compartments shows that they are comparable in size. Scale bars, 20 μm.

In this study, we present an approach that merges lipid vesicles and copolymer-stabilized droplets to generate mechanically and chemically stable cell-like compartments, which we have called droplet-stabilized GUVs (dsGUVs). These compartments can be sequentially loaded with biomolecules by means of pico-injection technology and offer a well-defined micro-environment for a real step-by-step bottom-up assembly of intracellular modules with desired features. Moreover, the model systems were released from the oil phase and stabilizing droplets after assembly, thus paving the way towards interactions of these synthetic cells with physiologically relevant environments such as extracellular matrices, cells or signalling proteins.

Formation of dsGUVs and their analysis

Droplet-based microfluidics allows for high-throughput generation of monodisperse droplets, thus enabling the precise estimation of the lipid concentration required for the formation of a continuous lipid bilayer at the droplets' inner interface of the polymer shell (Supplementary Note 1 and Supplementary Fig. 1). The determined optimal amount (800 μM) of various lipid compositions in the form of LUVs or GUVs was dissolved in Milli-Q water and encapsulated into copolymer-stabilized droplets of 40 μm diameter (Supplementary Methods). The lipid-containing droplets are shown in Fig. 1a,b. To transform the encapsulated vesicles into a continuous supported lipid bilayer at the droplets' inner interface, a solution with optimized $MgCl_2$ concentration of 10 mM was introduced during droplet production or by means of pico-injection (Supplementary Methods). In the case of droplets containing LUVs, the formation of the continuous lipid bilayer was detected within a few seconds. The formation of a dsGUV out of the GUVs was considerably slower (in the range of 30 min) due to the slow diffusion of the GUVs towards the droplets' interface (Supplementary Note 2 and Supplementary Movie 1). Mg^{2+} ions are considered to be the most efficient mediators of lipid vesicle

Table 1 | Lipid diffusion coefficients obtained by FRAP measurements.

Lipid composition	D ($\mu m^2 s^{-1}$)	Lipid-based compartment
DOPC:DOPE:DOPS(8:1:1), 1% ATTO488-DOPE	3.52 ± 0.26	GUV formed by electroformation and encapsulated into droplet
Egg PC:Egg PG (1:1), 1% ATTO488-DOPE	3.96 ± 0.51	GUV formed by electroformation and encapsulated into droplet
DOPC, 1% RhB-DOPE	4.42 ± 0.65	GUV formed by electroformation and encapsulated into droplet
DOPC:DOPE:DOPS(8:1:1), 1% ATTO488-DOPE	3.31 ± 0.77	dsGUV
Egg PC:Egg PG (1:1), 1% ATTO488-DOPE	2.88 ± 0.06	dsGUV
DOPC, 1% RhB-DOPE	4.11 ± 0.59	dsGUV
DOPC:Chol:DOPS(8:1:1), 1% ATTO488-DOPE	4.03 ± 0.56	dsGUV
DOPC:Chol:DOPS(8:1:1), 1% ATTO488-DOPE	4.24 ± 0.94	Released lipid compartment
DOPC:Chol:DOPS(8:1:1), 1% ATTO488-DOPE	4.43 ± 1.23	GUV formed by electroformation

rupture, because they promote adhesion to a supporting surface[10,26]. It is worth mentioning that neither the addition of Ca^{2+} (10 mM) nor lower concentrations of Mg^{2+} (1 mM) as tested using the same lipid concentration could obtain comprehensive vesicle fusion to the droplets' inner surface (Supplementary Fig. 2).

To assess the formation process and the dynamics of the assembled dsGUV lipid bilayer, fluorescence intensity analyses, fluorescence recovery after photobleaching (FRAP) measurements, and the release of GUVs from the stabilizing droplet shell were performed. The insets in Fig. 1b show representative fluorescence intensity profiles of the encapsulated GUVs and the dsGUVs (both with identical lipid compositions), evaluated with a laser scanning confocal microscope using the same acquisition conditions (Methods). A fit to the profile revealed similar integrated intensity values of 42 ± 8 and 44 ± 4 (arbitrary intensity units) for dsGUVs and encapsulated GUVs, respectively. These findings may indicate a similar lipid density for dsGUVs and GUVs.

FRAP measurements (Table 1) revealed slightly lower lipid mobility in dsGUVs compared to encapsulated free-standing GUVs (Supplementary Methods and Supplementary Note 3). This can be attributed to the fact that the supported lipid membrane is subject to perturbations from the inner interface of the copolymer-stabilized droplet. Previous reports found a similar or an even lower diffusion coefficient for planar supported lipid membranes in comparison to free-standing GUVs[27,28].

Importantly, a microfluidic release device was developed to transfer the assembled lipid compartments into a physiologically relevant, aqueous phase (Fig. 1c, Methods). The release of the assembled lipid compartments (Methods) from the stabilizing polymer droplets into the aqueous phase is shown in Fig. 1c. As can be observed from the fluorescence images, the diameter of the released GUVs (26.2 ± 1.2 μm) in the aqueous phase is slightly smaller compared to that of the dsGUV prior to release (28.3 ± 0.6 μm). A slight shrinkage of the released GUVs can be explained by the change of the osmotic balance. FRAP measurements performed on the released GUVs and on those formed by traditional electroformation (consisting of the same lipid composition) revealed similar lipid mobility (Table 1).

Biofunctionalization of dsGUVs

To test the ability of the dsGUVs to serve as anchoring points for the immobilization of (His-tag) proteins, a lipid solution consisting of 9:1 DOPC:DGS-NTA(Ni) (220 μM) and (His6)-GFP was encapsulated into copolymer-stabilized droplet shells (Methods). The analysis of the fluorescence images of the (His6)-GFP inside the dsGUVs revealed the localization of the fluorescence signal at the periphery of the dsGUV—in other words, the same place at which the anchor DGS-NTA(Ni^{2+}) lipids are situated (Supplementary Fig. 3a). In contrast, a homogeneously distributed fluorescence signal was observed inside non-functionalized dsGUVs (Supplementary Fig. 3b).

FRAP measurements were performed to assess the kinetics of diffusion within the GFP-linked copolymer-stabilized droplets[21] and the GFP-linked dsGUVs (Supplementary Fig. 3c). Data analysis revealed diffusion coefficients of 1.22 ± 0.03 and 0.20 ± 0.05 $\mu m^2 s^{-1}$ for proteins linked to the lipid bilayer or to the polymer membrane, respectively.

Sequential assembly of sub-cellular units into the dsGUVs

To construct cellular modules by means of bottom-up assembly, an automated microfluidic approach was adapted to allow for the sequential loading of various sub-cellular functional units into the dsGUVs. Towards this end, we incorporated transmembrane proteins (integrin and ATP synthase) and cytoskeletal proteins (G-actin and tubulin) into the dsGUVs (Fig. 2).

Following the formation of the dsGUVs, we used a pico-injection system[24] to inject and to fuse transmembrane protein-containing proteoliposomes, that is, liposomes containing TAMRA-labelled $\alpha_{IIb}\beta_3$ integrin or Alexa 488-labelled F_oF_1-ATP synthase (Methods), with the dsGUVs composed of 8:1:1 DOPC:DOPE:DOPS. Lipid labelling was obtained by adding either 1% ATTO 488-labelled DOPE or 1% Rhodamine B (RhB)-labelled DOPE. The co-localization of the integrin or the F_oF_1-ATP synthase with the lipid fluorescence signals is shown in Fig. 3a, indicating the successful fusion of the proteoliposomes with the dsGUVs. As a control, we injected F_oF_1-ATP synthase into copolymer-stabilized droplets without any dsGUVs, and mixed these droplets with dsGUVs containing F_oF_1-ATP synthase. It should be noted that only within the dsGUV was the F_oF_1-ATP synthase fused with the periphery. In the case of droplets without dsGUVs, F_oF_1-ATP synthases were distributed homogeneously within the entire droplet. Similar results were obtained for integrin. This clearly indicates that transmembrane proteins such as F_oF_1-ATP synthase or integrin need the formation of a dsGUV to fuse with the lipid bilayer on the droplet periphery.

FRAP measurements of transmembrane proteins reconstituted into dsGUVs revealed diffusion coefficients of 1.20 ± 0.7 and 0.70 ± 0.1 $\mu m^2 s^{-1}$ for F_oF_1-ATP synthase and integrin, respectively. This value is in good agreement with previously published studies on integrin $\alpha_{IIb}\beta_3$ mobility in planar supported lipid bilayers and in cellular membranes[29–31]. Moreover, to test the functionality of the reconstituted integrin, RGD peptides anchored to gold-linked surfactants[21,32] (Methods) were used to provide binding sites for integrin adhesion (Fig. 3b). In this case, the diffusion coefficient of integrin dropped to 0.13 ± 0.03 $\mu m^2 s^{-1}$, consistent with the mobility of the copolymer surfactant layer that stabilizes the droplet. Successful binding between the integrin and the RGD on the droplet interface indicates the functional incorporation of integrin into the lipid bilayer of the dsGUVs. It also reveals that at least some of the integrin proteins are oriented correctly, with their extracellular parts pointing towards the inner interface of the copolymer-stabilized droplet. It should be mentioned that the establishment of a methodology for integrating membrane proteins into lipid bilayers

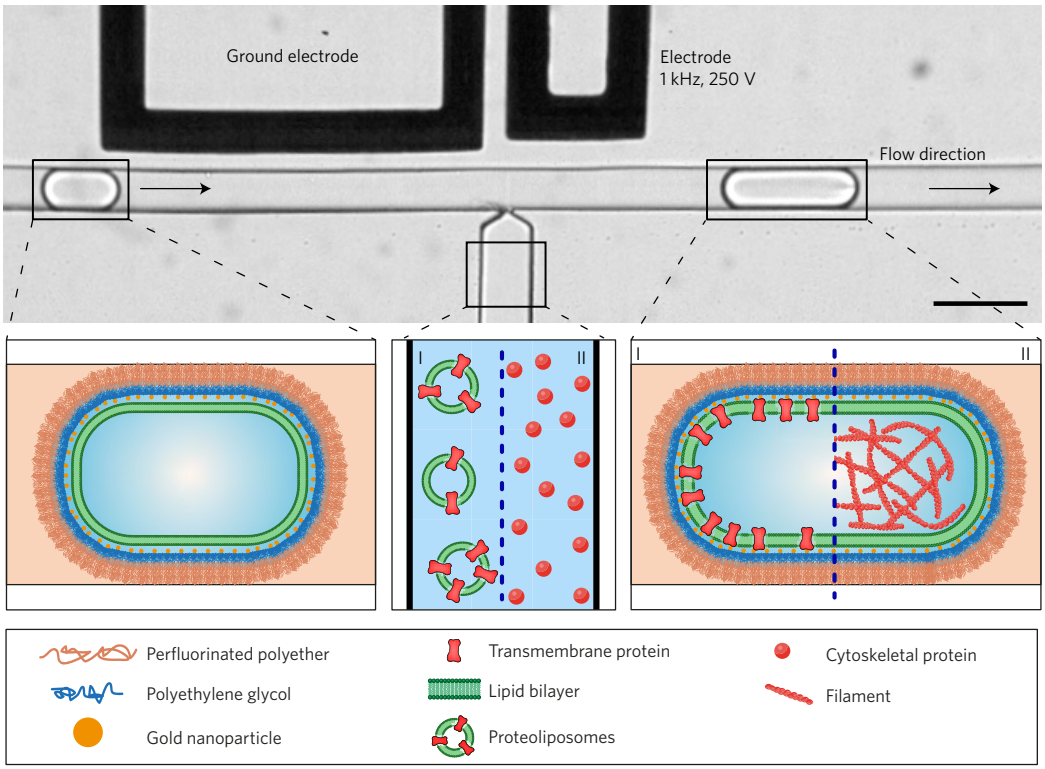

Figure 2 | Sequential bottom-up assembly of dsGUV cell-like compartments. Schematic representation of the process for incorporating transmembrane and cytoskeletal proteins into dsGUVs by means of high-throughput droplet-based pico-injection technology. Scale bar, 50 μm.

with a specific orientation is not in the scope of this work, but is an important task for future studies.

For the activity assessment of the reconstituted F_oF_1-ATP synthase in dsGUVs, an acidic FC-40 oil was added to the oil phase. This addition resulted in the establishment of a transmembrane pH gradient (ΔpH) as a driving force for ATP synthesis inside the droplets (Methods and Fig. 3c). Following 2 min incubation time, the aqueous content of the dsGUVs was released and the synthesized ATP concentration was determined by means of bioluminescence luciferase in a plate reader (Methods). A total amount of 5 nM ATP was measured in the released solution (Fig. 3c and Methods), which indicates the functional reconstitution of the F_oF_1-ATP synthases in the dsGUVs. It also reveals that at least some of the F_oF_1-ATP synthases are oriented correctly—that is, the F_1 portion is pointing towards the inside of the dsGUV. The low concentration of synthesized ATP can be attributed to the lack of a sufficient transmembrane electric potential gradient[33]. Moreover, the time delay between generating the proton motive force for ATP synthesis and the determination of the produced ATP was long so that enzyme-catalysed and pH-dependent ATP hydrolysis could reduce the amount of the remaining ATP. The drop of ATP over time as measured in the plate reader is attributed to the kinetic instability of ATP (Fig. 3c).

The same pico-injection approach was applied to obtain a bottom-up reconstitution of the actin cytoskeleton or microtubules within the dsGUVs (Methods). Towards this end, we proceeded by the following two-step process: the formation of dsGUVs (90% DOPC, 9% DOPS and 1% RhB-DOPE) in the presence of an actin or tubulin polymerization buffer; the pico-injection of G-actin (10 μM final concentration, including 1% Alexa 488-labelled G-actin) or tubulin (10 μM final concentration, including 10% ATTO 488-labelled tubulin) solution into the dsGUVs. Moreover, we compared this pico-injection approach to the premixed (one-step) approach, in which G-actin or tubulin proteins were mixed with LUVs prior to droplet formation (Methods).

The successful reconstitution of the actin filaments and microtubules within the dsGUVs could be obtained by sequential pico-injection only (Fig. 3d, middle panel). When using the one-step premixed approach, vesicle fusion to the droplets' inner surface was suppressed. In the case of microtubules none, and in the case of F-actin only partial fusion, was observed (Fig. 3d, top panel). The inability to form dsGUVs in the presence of microtubules is related to the fact that LUVs are subject to perturbations stemming from the amphiphilic nature of tubulin[34]. The sequential pico-injection approach enables the prior formation of stable dsGUVs with appropriate ionic conditions followed by the injection of proteins without perturbing the lipid bilayer of the dsGUVs.

Release of GUVs into physiological environments

To pave the way towards investigations of protocell interactions with physiological environments, we developed both a bulk and a microfluidic method to release assembled GUVs with or without proteins from the oil phase and stabilizing droplet shell to the water phase (Methods). By dissolving distinctive fluorophores in the oil phase as well as the enclosed and continuous aqueous phase, we could validate that the lipid membrane remains fully intact and impervious during the release process and that no oil residue could be detected in the water phase or the released GUVs (Supplementary Fig. 6). Moreover, to assess the purity of the GUVs, Raman spectra were collected on released GUVs (Supplementary Methods and Supplementary Fig. 7). As can be observed, no oil/surfactants were detected in the Raman spectra of the released GUVs. Additionally, by means of fluctuation analysis we calculated the bending rigidity values ($21.5 \pm 3.4 k_B T$) of released GUVs (Supplementary Methods). This value lies in the range of typical values reported for the bending rigidity of PC membranes[35], suggesting that the bilayers are clean of impurities. Moreover, these values correlate strongly with the bending rigidity values ($25.3 \pm 3.0 k_B T$) of the GUVs, consisting of the same lipid composition and formed by a standard electroformation method (Supplementary Methods).

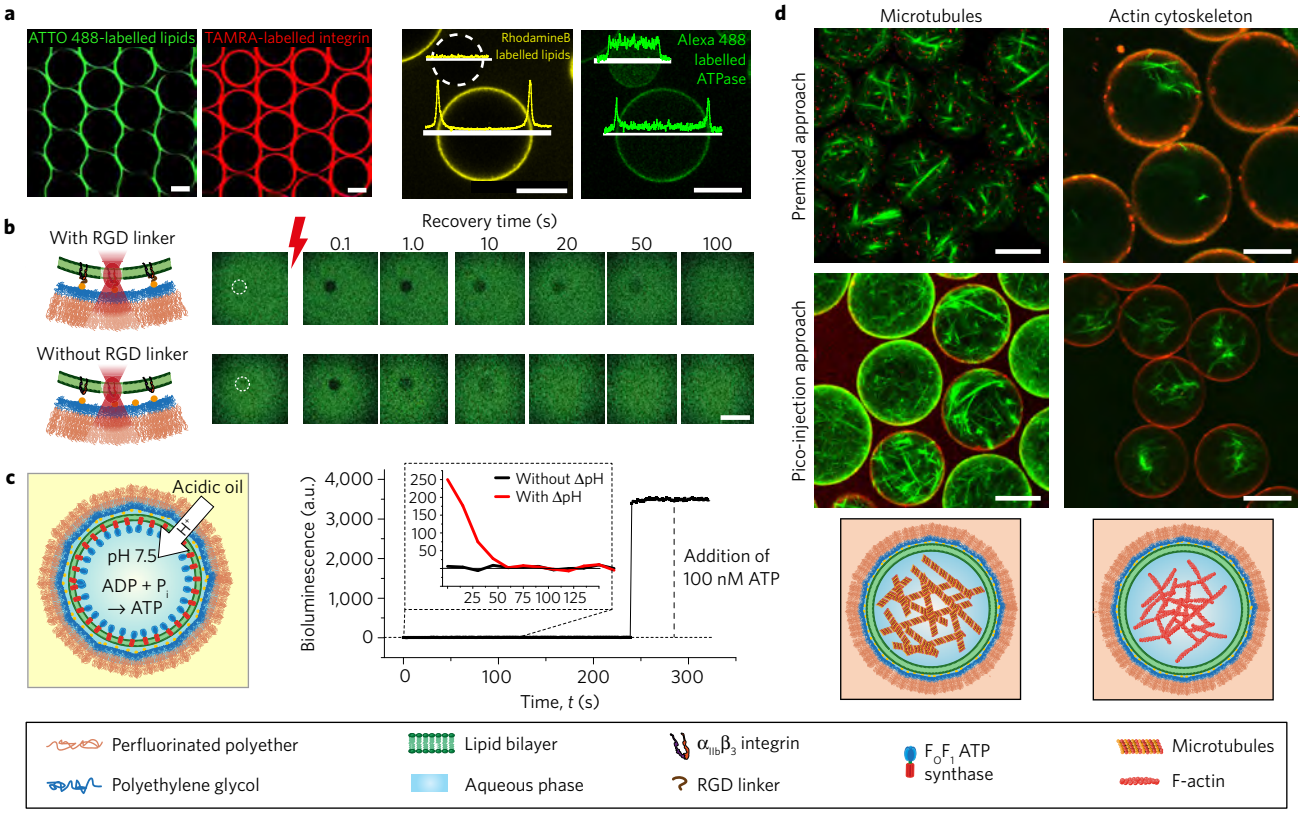

Figure 3 | Incorporation of transmembrane and cytoskeletal proteins into the dsGUV compartments by pico-injection technology. a, The left and right pair of images show representative fluorescence images of the same areas of observation after pico-injection of integrin-containing liposomes (ATTO 488-labelled DOPE lipids in green and TAMRA-labelled $\alpha_{IIb}\beta_3$ integrin in red) and of F_oF_1-ATP synthase-containing liposomes into the dsGUVs (RhB-labelled DOPE lipids in yellow and Alexa 488-labelled F_oF_1-ATP synthase in green), respectively. Superimposed on the right pair of images is the fluorescence intensity profile. Lipids and F_oF_1-ATP synthases clearly co-localize in dsGUVs. Without an inner dsGUV (white dashed circle), the signal from the Alexa 488-labelled F_oF_1-ATP synthase is equally distributed within the droplet. Scale bars, 20 μm. **b**, Schematic illustration and representative results of FRAP measurement of labelled integrin with (top row) and without (bottom row) immobilization to the gold-linked surfactants via RGD peptides. The focus area of the light source is encircled in the pre-bleach frame and the timeline on top indicates when follow-up images were taken. Scale bar, 10 μm. **c**, Schematic illustration of F_oF_1-ATP synthase-reconstituted dsGUVs and of the transmembrane pH gradient—the driving force of ATP synthesis—as achieved by the addition of acidic FC-40 oil. The right graph shows the bioluminescence intensity response to the ATP content as a function of time. The insert shows the representative bioluminescence intensity curves obtained from the aqueous content of dsGUVs activated (red) by a pH gradient and dsGUVs without a pH gradient (black). The bioluminescence curve was calibrated by the addition of 100 nM ATP solution. **d**, Representative fluorescence images of microtubules (10% ATTO 488-labelled tubulin, left panel) or the actin cytoskeleton (1% Alexa 488-labelled actin, right panel) in droplets containing RhB-labelled DOPE lipids, as obtained by either the premixed (top) or the pico-injection approach (bottom). Scale bar, 20 μm.

To demonstrate the interactions of the released protocells with physiological environments, Fig. 4 shows optical micrographs of integrin $\alpha_{IIb}\beta_3$- or F-actin-containing dsGUVs and their corresponding protocells in the aqueous phase after release. To validate the functionality of the reconstituted integrin $\alpha_{IIb}\beta_3$, the spreading behaviour of the released integrin $\alpha_{IIb}\beta_3$-functionalized GUVs is investigated. While these integrin $\alpha_{IIb}\beta_3$-protocells do not spread on BSA-coated interfaces, they spread well on fibrinogen but less on fibronectin or collagen matrices as is expected from the platelet adhesion receptor integrin $\alpha_{IIb}\beta_3$ (Fig. 4b and Supplementary Methods and Supplementary Fig. 8; refs 32,36). The differential adhesion on the various matrices further demonstrates that the protein reconstitution and release process does not affect the biological functionality of the synthetic cells.

In conclusion, the developed technology overcomes fundamental limitations associated with the formation and manipulation of currently existing protocells or polymersomes for the design of complex synthetic cells. Recently developed microfluidic methods showed remarkable success with the high-throughput formation of monodisperse GUVs[37–39]. Moreover, a control over the GUV lipid composition and its asymmetry was achieved by microfluidic methods such as layer-by-layer lipids assembly[40], pulse-jet[41] and droplet shooting[42]. Despite the progress made in recent years in designing protocells, the major drawback of all of these methods is a lack of ability to sufficiently manipulate the protocell content sequentially. The assembly of a cell-like compartment with distinct functionality requires the combination of different proteins, molecules and buffer conditions that are incompatible when applied to the same spatial confinement all at once. The formation of dsGUVs enables the generation of mechanically and chemically stable compartments which can be loaded sequentially with different proteins and molecules using pico-injection technology. This sequential procedure allows for a combination of molecules and organized molecular structures that would not occur spontaneously. These system properties lay the groundwork for realizing a real bottom-up assembly of rather complex combinations and functions in synthetic compartments. Importantly, the ability to release functional protocells from the stabilizing droplets into water phase paves the way towards investigations of interactions of synthetic cells with physiologically relevant environments such as given by extracellular matrices, cells, viruses or signalling molecules. Finally, it is worthwhile mentioning that the formation of synthetic cells by this technology is a

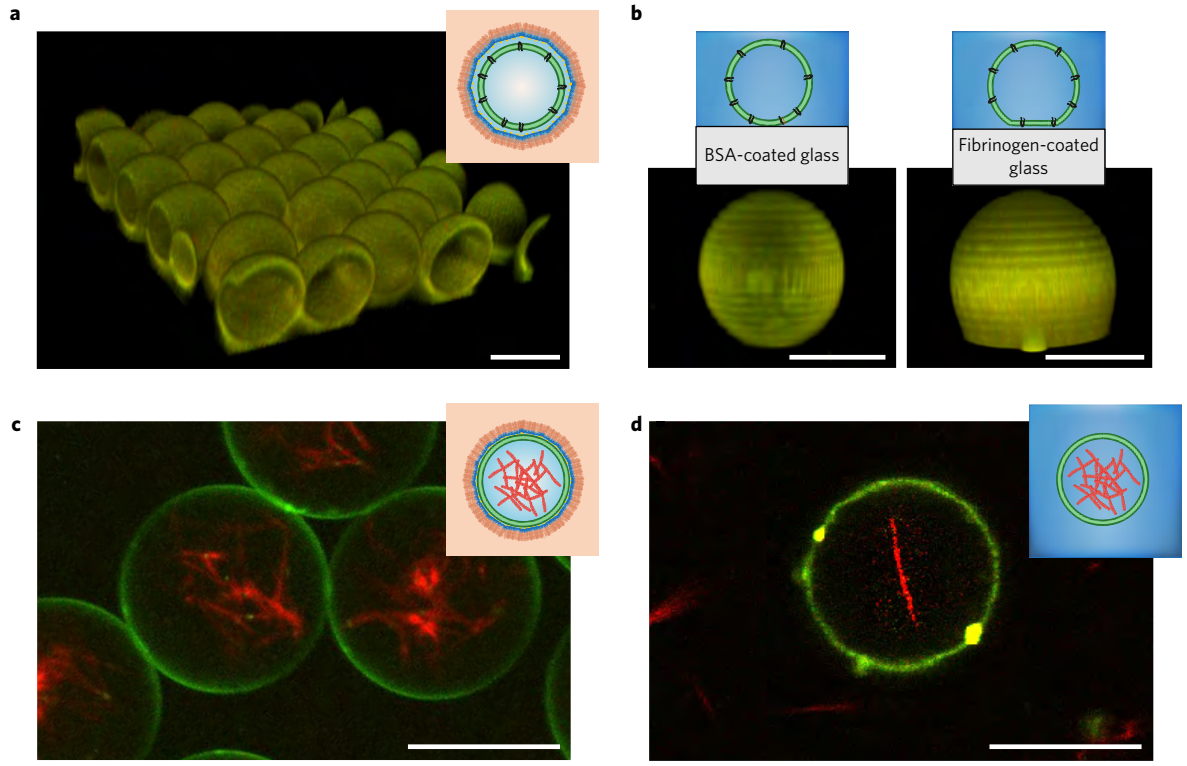

Figure 4 | Release of actin- and integrin-reconstituted GUVs. a,**b**, Representative 3D reconstitution of confocal images of dsGUVs with reconstituted integrin (**a**) and released lipid compartments with reconstituted integrin in contact with BSA- (left image) and fibrinogen-coated (right image) glass surfaces (**b**). The merged fluorescence signals include both ATTO 488-labelled DOPE lipids and TAMRA-labelled $\alpha_{IIb}\beta_3$ integrin. **c**,**d**, Representative fluorescence images of the actin cytoskeleton-containing dsGUVs (**c**) and of the released actin cytoskeleton-containing lipid compartments (**d**). The fluorescence signals correspond to Alexa 488-labelled actin (red) and RhB-labelled DOPE lipids (green). Scale bar, 20 μm.

high-throughput method enabling the generation of up to 10^3 functional compartments per second. As a result, it generates a vast number of synthetic cells of unique and precise composition, which can be applied for follow-up scientific and technological applications.

Methods

Methods, including statements of data availability and any associated accession codes and references, are available in the online version of this paper.

Received 6 June 2016; accepted 12 September 2017; published online 16 October 2017

References

1. Szostak, J. W., Bartel, D. P. & Luisi, P. L. Synthesizing life. *Nature* **409,** 387–390 (2001).
2. Tawfik, D. S. & Griffiths, A. D. Man-made cell-like compartments for molecular evolution. *Nat. Biotechnol.* **16,** 652–656 (1998).
3. Diekmann, Y. & Pereira-Leal, J. B. Evolution of intracellular compartmentalization. *Biochem. J.* **449,** 319–331 (2013).
4. Agapakis, C. M., Boyle, P. M. & Silver, P. A. Natural strategies for the spatial optimization of metabolism in synthetic biology. *Nat. Chem. Biol.* **8,** 527–535 (2012).
5. Yoshida, M., Muneyuki, E. & Hisabori, T. ATP synthase—A marvellous rotary engine of the cell. *Nat. Rev. Mol. Cell Biol.* **2,** 669–677 (2001).
6. Geiger, B., Spatz, J. P. & Bershadsky, A. D. Environmental sensing through focal adhesions. *Nat. Rev. Mol. Cell Biol.* **10,** 21–33 (2009).
7. Nomura, S. M. *et al*. Gene expression within cell-sized lipid vesicles. *Chembiochem* **4,** 1172–1175 (2003).
8. Merkle, D., Kahya, N. & Schwille, P. Reconstitution and anchoring of cytoskeleton inside giant unilamellar vesicles. *Chembiochem* **9,** 2673–2681 (2008).
9. Hardy, G. J., Nayak, R. & Zauscher, S. Model cell membranes: techniques to form complex biomimetic supported lipid bilayers via vesicle fusion. *Curr. Opin. Colloid Interface Sci.* **18,** 448–458 (2013).
10. Seantier, B. & Kasemo, B. Influence of mono- and divalent ions on the formation of supported phospholipid bilayers via vesicle adsorption. *Langmuir* **25,** 5767–5772 (2009).
11. Shigematsu, T., Koshiyama, K. & Wada, S. Effects of stretching speed on mechanical rupture of phospholipid/cholesterol bilayers: molecular dynamics simulation. *Sci. Rep.* **5,** 15369 (2015).
12. Jorgensen, I. L., Kemmer, G. C. & Pomorski, T. G. Membrane protein reconstitution into giant unilamellar vesicles: a review on current techniques. *Eur. Biophys. J.* **46,** 103–119 (2016).
13. Discher, B. M. *et al*. Polymersomes: tough vesicles made from diblock copolymers. *Science* **284,** 1143–1146 (1999).
14. Palivan, C. G. *et al*. Bioinspired polymer vesicles and membranes for biological and medical applications. *Chem. Soc. Rev.* **45,** 377–411 (2016).
15. Onaca, O., Nallani, M., Ihle, S., Schenk, A. & Schwaneberg, U. Functionalized nanocompartments (Synthosomes): limitations and prospective applications in industrial biotechnology. *Biotechnol. J.* **1,** 795–805 (2006).
16. Picker, A., Nuss, H., Guenoun, P. & Chevallard, C. Polymer vesicles as microreactors for bioinspired calcium carbonate precipitation. *Langmuir* **27,** 3213–3218 (2011).
17. Lee, J. C. M., Santore, M., Bates, F. S. & Discher, D. E. From membranes to melts, rouse to reptation: diffusion in polymersome versus lipid bilayers. *Macromolecules* **35,** 323–326 (2002).
18. Duncombe, T. A., Tentori, A. M. & Herr, A. E. Microfluidics: reframing biological enquiry. *Nat. Rev. Mol. Cell Biol.* **16,** 554–567 (2015).
19. Martino, C. & deMello, A. J. Droplet-based microfluidics for artificial cell generation: a brief review. *Interface Focus* **6,** 20160011 (2016).
20. Schaerli, Y. *et al*. Continuous-flow polymerase chain reaction of single-copy DNA in microfluidic microdroplets. *Anal. Chem.* **81,** 302–306 (2009).
21. Platzman, I., Janiesch, J.-W. & Spatz, J. P. Synthesis of nanostructured and biofunctionalized water-in-oil droplets as tools for homing T cells. *J. Am. Chem. Soc.* **135,** 3339–3342 (2013).
22. Huebner, A. *et al*. Quantitative detection of protein expression in single cells using droplet microfluidics. *Chem. Commun.* **12,** 1218–1220 (2007).
23. Janiesch, J. W. *et al*. Key factors for stable retention of fluorophores and labeled biomolecules in droplet-based microfluidics. *Anal. Chem.* **87,** 2063–2067 (2015).

24. Abate, A. R., Hung, T., Mary, P., Agresti, J. J. & Weitz, D. A. High-throughput injection with microfluidics using picoinjectors. *Proc. Natl Acad. Sci. USA* **107,** 19163–19166 (2010).
25. Itel, F. *et al*. Molecular organization and dynamics in polymersome membranes: a lateral diffusion study. *Macromolecules* **47,** 7588–7596 (2014).
26. Bhatia, T., Husen, P., Ipsen, J. H., Bagatolli, L. A. & Simonsen, A. C. Fluid domain patterns in free-standing membranes captured on a solid support. *Biochim. Biophys. Acta Biomembr.* **1838,** 2503–2510 (2014).
27. Machan, R. & Hof, M. Lipid diffusion in planar membranes investigated by fluorescence correlation spectroscopy. *Biochim. Biophys. Acta* **1798,** 1377–1391 (2010).
28. Przybylo, M. *et al*. Lipid diffusion in giant unilamellar vesicles is more than 2 times faster than in supported phospholipid bilayers under identical conditions. *Langmuir* **22,** 9096–9099 (2006).
29. Goennenwein, S., Tanaka, M., Hu, B., Moroder, L. & Sackmann, E. Functional incorporation of integrins into solid supported membranes on ultrathin films of cellulose: impact on adhesion. *Biophys. J.* **85,** 646–655 (2003).
30. Erb, E. M., Tangemann, K., Bohrmann, B., Muller, B. & Engel, J. Integrin alpha IIb beta 3 reconstituted into lipid bilayers is nonclustered in its activated state but clusters after fibrinogen binding. *Biochemistry* **36,** 7395–7402 (1997).
31. Edel, J. B., Wu, M., Baird, B. & Craighead, H. G. High spatial resolution observation of single-molecule dynamics in living cell membranes. *Biophys. J.* **88,** L43–L45 (2005).
32. Frohnmayer, J. P. *et al*. Minimal synthetic cells to study integrin-mediated adhesion. *Angew. Chem. Int. Ed.* **54,** 12472–12478 (2015).
33. Fischer, S. & Graber, P. Comparison of Delta pH- and Delta phi-driven ATP synthesis catalyzed by the H+-ATPases from *Escherichia coli* or chloroplasts reconstituted into liposomes. *FEBS Lett.* **457,** 327–332 (1999).
34. Wolff, J. Plasma membrane tubulin. *Biochim. Biophys. Acta Biomembr.* **1788,** 1415–1433 (2009).
35. Dimova, R. Recent developments in the field of bending rigidity measurements on membranes. *Adv. Colloid Interface Sci.* **208,** 225–234 (2014).
36. Streicher, P. *et al*. Integrin reconstituted in GUVs: a biomimetic system to study initial steps of cell spreading. *Biochim. Biophys. Acta Biomembr.* **1788,** 2291–2300 (2009).
37. Karamdad, K., Law, R. V., Seddon, J. M., Brooks, N. J. & Ces, O. Preparation and mechanical characterisation of giant unilamellar vesicles by a microfluidic method. *Lab Chip* **15,** 557–562 (2015).
38. Matosevic, S. & Paegel, B. M. Stepwise synthesis of giant unilamellar vesicles on a microfluidic assembly line. *J. Am. Chem. Soc.* **133,** 2798–2800 (2011).
39. Deng, N.-N., Yelleswarapu, M. & Huck, W. T. S. Monodisperse uni- and multicompartment liposomes. *J. Am. Chem. Soc.* **138,** 7584–7591 (2016).
40. Matosevic, S. & Paegel, B. M. Layer-by-layer cell membrane assembly. *Nat. Chem.* **5,** 958–963 (2013).
41. Kamiya, K., Kawano, R., Osaki, T., Akiyoshi, K. & Takeuchi, S. Cell-sized asymmetric lipid vesicles facilitate the investigation of asymmetric membranes. *Nat. Chem.* **8,** 881–889 (2016).
42. Morita, M. *et al*. Droplet-shooting and size-filtration (DSSF) method for synthesis of cell-sized liposomes with controlled lipid compositions. *ChemBioChem* **16,** 2029–2035 (2015).

Acknowledgements

Parts of the research leading to these results have received funding from the European Research Council/ERC Grant Agreement no. 294852, SynAd. This work is also part of the MaxSynBio consortium, which is jointly funded by the Federal Ministry of Education and Research of Germany and the Max Planck Society. The work was also partly supported by the SFB 1129 of the German Science Foundation and the VolkswagenStiftung (priority call 'Life?'). J.P.S. is the Weston Visiting Professor at the Weizmann Institute of Science and part of the excellence cluster CellNetworks at the University of Heidelberg. J.-C.B. acknowledges financial support by the ERC (FP7/2007-2013/ERC Grant agreement 306385-SofI). I.P. acknowledges the support of the Alexander von Humboldt Foundation. The authors acknowledge the help of P. Gruner and B. Riechers for their technical assistance with preliminary microfluidic experiments and A. Richter (WITec GmbH, Germany) for her technical assistance with Raman microscopy. The support of N. Grunze for editing the manuscript as well as of J. Ricken and Ch. Mollenhauer for their general support in protein purification and chemical synthesis is highly acknowledged. The Max Planck Society is appreciated for its general support in all aspects of our research.

Author contributions

M.W. and J.P.F. realized experimentally the general concept of dsGUVs by microfluidic technology, established pico-injection technology and its application for the design of synthetic cells—this includes the formation of dsGUVs, release of GUVs from oil to water phase, FRAP measurements—and wrote parts of the manuscript. M.W. performed microtubule assembly and integration of functional ATP synthase and its analysis; J.P.F. reconstituted functional Integrin in liposomes and dsGUV and performed release of Integrin GUVs from oil to water phase; L.T.B. optimized the release of GUVs from oil to water phase, in particular the release of integrin functionalized GUVs, performed adhesion experiments of integrin functionalized GUVs to different matrices, and wrote parts of the manuscript; B.H. performed the experiments of dsGUVs with F-actin and its release from oil to water phase and performed Raman spectroscopy analysis; J.-W.J. performed the experiments of dsGUVs with F-actin and synthesized polymer-based surfactants; T.H. and M.B. prepared the labelled F_oF_1-ATP synthase, R.B.L., R.D. and R.L. developed and discussed lipid bilayer formation using droplets, E.B. and J.-C.B. helped install the pico-injection technology, T.V.-K. and K.S. supported the reconstitution of F_oF_1-ATP synthase, I.P. designed and supervised the experiments, and wrote the manuscript; J.P.S. invented the concept of synthetic cell formation by sequential bottom-up assembly in droplet-stabilized compartments, designed, supervised and managed the experiments, and wrote the manuscript.

Additional information

Supplementary information is available in the online version of the paper. Reprints and permissions information is available online at www.nature.com/reprints. Publisher's note: Springer Nature remains neutral with regard to jurisdictional claims in published maps and institutional affiliations. Correspondence and requests for materials should be addressed to I.P. or J.P.S.

Competing financial interests

The authors declare no competing financial interests.

Methods

Fluorescence intensity analysis. To compare the lipid membrane fluorescence intensity of encapsulated GUVs to that of dsGUVs with the same lipid composition (1:1 Egg PC:Egg PG, including 0.5% ATTO488-DOPE), the droplets were evaluated back-to-back, preserving identical settings with a Leica SP5 confocal microscope (Supplementary Methods). More than twenty intensity profiles were extracted for each droplet type using Fiji/ImageJ. Fluorescence analysis of the encapsulated GUVs revealed a reduction in the amplitude and a broadening of the fluorescence intensity profile peak in proximity to the copolymer-stabilized droplet interface (Fig. 1b). This is due to refraction and diffraction at the water–oil phase barrier. To compare the fluorescence intensities, a Gaussian function with a background correction was fitted to the intensity profile peaks using a nonlinear least-squares fit (Matlab 2015 SP1).

Microfluidic release device. A high-throughput microfluidic device was developed to release assembled lipid compartments from the stabilizing polymer droplet shells into the aqueous phase (Fig. 1c). All flows inside the device were controlled by a microfluidic flow control system (MFCS-EZ, Fluigent). To minimize shear forces, the height of the channels was designed to exceed the droplet diameter, and the pressure in the inlet channels was adjusted to a maximum of 20 mbar with minor corrections for individual devices and experimental conditions. The dsGUVs were injected into the inlet channel of the release device and isolated at the T-junction where a tributary oil flow containing 20 vol% perfluoro-1-octanol destabilizing surfactants (Sigma-Aldrich) joins. The total flow was adjusted to allow efficient time for the destabilizing surfactants to replace and displace stabilizing surfactants prior to reaching the release unit. In this unit, the dsGUVs encounter the aqueous phase in a wide perpendicular channel. To minimize the mechanical impact on the droplets at the oil/water junction, the droplets were decelerated using passive trapping structures within the microfluidic channels (that is, rows of pillars separated by distances smaller than the representative droplet dimensions), which we designed for this purpose (Supplementary Movie 2)[43].

To avoid oil penetrating into the aqueous channel whenever there were no droplets in the trapping structures, the aqueous flow was adjusted to achieve a zero-pressure gradient at the oil/water junction. As a result, the oil flows into the adjacent oil outlet channels without droplets blocking the slits. Whenever a droplet enters, it blocks the first slits on both sides, thereby increasing the pressure. As the droplet flows along the passive trapping structures, it passes pairs of slits, opening these up for oil flow to the oil outlet channels. With each pair of slits that opens up, the channel cross section for the oil flow to the adjacent oil channels increases, subsequently decreasing the pressure that is pushing the droplet along the channel. The droplet decelerates as it approaches the oil–water interface. Upon contact with the aqueous phase, the residual surfactant layer peels off the droplet's polymer shell, which flows to the oil outlet channel. This releases the droplet's aqueous content (including the lipid compartments) into the aqueous phase with the appropriate ionic conditions.

Lipid composition for release. The release efficiency of GUVs was found to be dependent on the lipid composition. A few general key factors for the stability of lipid bilayers have been identified. First, for better stability of self-supporting released GUVs 10–20 mol% cholesterol was included (C8667, Sigma-Aldrich) for the release experiments. The lipid composition used for the results presented in Fig. 1c, consisted of a molar ratio of 4:4:2 of DOPC, POPC and cholesterol, respectively and included 0.5% Atto488-DOPE for observation. Second, in the case of negatively charged GUVs, release efficiency was affected when lipid compositions exceeded a net concentration of 10 mol% of negatively charged lipids. Therefore, the optimized lipid composition for the release experiments of negatively charged GUVs consisted of a molar ratio of 1:8:1 of DOPG, DOPC and cholesterol, respectively.

RGD-peptide immobilization to the gold-linked surfactants. To provide integrin adhesion sites inside the gold-nanostructured droplets, a two-step method to immobilize SN528 RGD peptides[32] (kindly provided by Kessler's group from TU Munich) on gold nanoparticles via its thiol linker was followed[21]. The freeze-dried Au-PEG(436 g mol^{-1})-PFPE(7,000 g mol^{-1}) diblock-copolymer surfactant was dissolved in 100 µl fluorinated FC-40 oil. Next, the aqueous RGD-peptide solution (50 µM, 100 µl) was added and everything was stirred for 1 h. To remove the unbound RGD peptides, the crude product solution was centrifuged. The supernatant solution was removed and the precipitant was freeze-dried for 24 h to completely remove the remaining water. Finally, the product was dissolved in 1 ml of FC-40 oil and filtered with a hydrophobic filter (PTFE 0.2 µm) to remove traces of unreacted peptide.

GFP immobilization. (His6)-GFP was a gift from S. Gardia, Addgene, plasmid #29663. The protein was expressed in *Escherichia coli* using standard protocols and purified by Ni-NTA chromatography. The linkage of (His6)-GFP to gold-linked surfactants via Ni-NTA-thiol was performed as previously described[21], with the exception that purified Milli-Q water (Millipore filtered) was used as the aqueous phase instead of PBS buffer. To link (His6)-GFP to the lipid bilayer, the following procedure was applied. $NiCl_2$ (9 µl, 100 mM, Fluka) was mixed with a water solution of DGS-NTA lipids (300 µl, 1 mM) and stirred for 20 min. LUVs produced from 9:1 DOPC:DGS-NTA(Ni) (220 µM) were encapsulated into copolymer-stabilized droplet shells (100 µm diameter). Following encapsulation, a water solution containing (His6)-GFP (10 µM) and $MgCl_2$ (10 mM) was pico-injected into the droplets to form GFP-linked dsGUVs.

Integrin purification labelling and reconstitution. Integrin $\alpha_{IIb}\beta_3$ was purified from outdated human blood platelets (Katharinenhospital Stuttgart) using TBS and Triton X-100 according to a previously reported protocol[32]. Affinity chromatography over Concanavalin A and Heparin columns was followed by gel filtration over a Superdex 200 Prep Grade column (GE Healthcare). The biological activity of the purified integrin was analysed by an enzyme-linked immunosorbent assay (ELISA) using AB1967 anti-integrin α_{IIb} antibodies (Merck Millipore). Following purification, integrin was stored at −80 °C in TRIS storage buffer, consisting of 20 mM TRIS/HCl pH 7.4, 150 mM NaCl, 1 mM $CaCl_2$, 1 mM $MgCl_2$, 0.1% (w/v) Triton X-100, 0.02% (w/v) NaN_3 and 2 mg ml^{-1} Aprotinin. Integrin $\alpha_{IIb}\beta_3$ was labelled with 5-(and-6)-carboxytetramethylrhodamine, succinimidyl ester, #C1171 TAMRA (Life Technologies) according to a previously published protocol[44]. A dye/protein ratio of 1.0 to 1.2 was measured by molecular dye extinction (ε_{555} = 80,000 mol^{-1}cm^{-1}). Functionality was measured with an ELISA binding assay.

Integrin reconstitution into the liposomes followed a previously published protocol[30]. In brief, 50 mol% of Egg PC and Egg PG were dried under a gentle stream of nitrogen and then placed under vacuum conditions overnight. Dried lipids were dissolved in 1 ml of TRIS buffer, consisting of 20 mM TRIS/HCl, pH 7.4, 50 mM NaCl, 0.5 mM $CaCl_2$ and 0.1% (w/v) Triton X-100, and integrin was added to a final 1:1,000 integrin–lipid ratio and incubated in the solution at 37 °C for 2 h. Triton X-100 was removed in two subsequent washing steps of 3.5 h each using 50 mg ml^{-1} BT Bio-Beads SM-2 (#152-8920, BIO-RAD). The size distribution of the liposomes and integrin-reconstituted proteoliposomes was measured by dynamic light scattering (DLS) in a Malvern Zetasizer (Nano ZS). Pico-injection technology was used to inject the integrin liposomes into the dsGUVs, which contained integrin activation buffer (20 mM TRIS/HCl, pH 7.4, 50 mM NaCl, 0.5 mM $CaCl_2$, 1 mM $MnCl_2$ and 1 mM $MgCl_2$). Theoretical estimation of the number of integrin proteins that might be reconstituted into dsGUVs is presented in Supplementary Note 4.

For the release of integrin-reconstituted GUVs from the stabilizing droplet shells, integrin was reconstituted into liposomes consisting of 100% EggPC. These proteoliposomes were mixed at a ratio of 1:9 with liposomes containing 4:3:2 DOPC:POPC:cholesterol including 1% ATTO 488-labelled DOPE and used for dsGUV formation.

F_oF_1-ATP synthase purification, labelling, reconstitution and activity assessment. The purification of F_oF_1-ATP synthase from *E. coli* and subsequent cysteine labelling at the C terminus of subunit *a* with Alexa 488 maleimide were performed according to the protocols described in Zimmermann *et al.*[45] and Heitkamp and colleagues[46]. Labelled (or unlabelled) F_oF_1-ATP synthase was reconstituted into preformed liposomes (~120 nm diameter) as described in Fischer and Gräber[33] and stored at −80 °C in tricine buffer, consisting of 20 mM tricine–NaOH (pH 8.0), 20 mM succinic acid, 0.6 mM KCl, 50 mM NaCl and 2.5 mM $MgCl_2$. Pico-injection technology was used to inject the F_oF_1-ATP synthase liposomes into the dsGUVs, which contained F_oF_1-ATP activity buffer, consisting of 20 mM tricine–NaOH (pH 7.5), 20 mM succinic acid, 10 mM $MgCl_2$, 5 mM NaH_2PO_4 and 50 µM ultra-pure ADP (Cell Technology).

For the activity assessment of the reconstituted F_oF_1-ATP synthase in dsGUVs the ATP synthase has to be energized by a transmembrane pH gradient established between the F_oF_1-ATP synthase-containing dsGUVs and the surrounding oil. To generate a pH gradient ($\Delta pH \approx 3$), 1µl of trifluoroacetic acid (TFA, 99%, Sigma-Aldrich) was dissolved in 1 ml FC-40 oil[47] and an oil exchange was performed. Following the application of the acidic oil, the change in the droplets' internal pH through proton diffusion was analysed by pyranine intensity detection (Supplementary Movie 3 and Supplementary Fig. 10)[48].

Following the reconstitution of the F_oF_1-ATP synthases in dsGUVs, 100 µl oil/dsGUVs solution was transferred to a 500 µl Eppendorf tube and 20 µl of acidic FC-40 oil was added by pipetting. The Eppendorf tube was carefully tilted and slowly rotated for 2 min. Then, 5 µl of perfluoro-1-octanol 20 vol% destabilizing surfactants (Sigma-Aldrich) was added to release the content of the droplets. To analyse the ATP content, 5 µl of the released aqueous solution was transferred to a well on a non-transparent 96-well plate with a flat bottom, containing 180 µl tricine buffer and 20 µl of 10-fold concentrated luciferase reagent (ATP Bioluminescence Kit CLS II, Sigma-Aldrich). A plate reader (Infinite M200, Tecan) was used to detect the bioluminescence intensity corresponding to the synthesized ATP in the aqueous solution. As a control, the same amount of aqueous solution was released

from the F_oF_1-ATP synthase-containing dsGUVs that were not energized by a transmembrane pH gradient and analysed. To assess the amount of synthesized ATP, a bioluminescence calibration curve was produced by the addition of 100 nM ATP solution.

Actin polymerization within dsGUVs. Actin was purchased from Cytoskeleton. Actin was stored in TRIS storage buffer, consisting of 2.0 mM TRIS/HCl pH 8, 0.2 mM $CaCl_2$, 0.2 mM ATP, 0.005% NaN_3 and 0.2 mM DTT, at −80 °C. Human recombinant fascin was purchased from Novubio (Bio-Techne), aliquoted and stored at −80 °C. 1% of Alexa 488-labelled actin (Life Technologies) was added to the non-labelled actin in all experiments to detect actin filament formation. To polymerize actin inside the dsGUVs, two methods were tested:

Premixed approach: Lipid and G-actin solutions were introduced via a microfluidic aqueous two-phase system (Supplementary Fig. 4C). To avoid polymerization prior to droplet formation, one aqueous phase contained 10 μM actin (1% Alexa 488-labelled actin) in storage buffer and the other aqueous phase contained the polymerization buffer (2.0 mM TRIS/HCl pH 8, 20 mM $MgCl_2$ 0.2 mM $CaCl_2$, 0.5 mM ATP, 0.005% NaN_3 and 0.2 mM DTT), 0.5 μM fascin and LUV solution consisting of 90% DOPC, 9% DOPS and 1% RhB-DOPE. The two aqueous phases were mixed during droplet generation at a flow-focusing junction (Supplementary Fig. 4).

Pico-injection approach: Two experimental steps were required for stable F-actin creation in dsGUVs. The first step entailed the creation of dsGUVs (90% DOPC, 9% DOPS and 1% RhB-DOPE) that contain actin polymerization buffer. The second step was the pico-injection of storage buffer containing G-actin (10 μM final concentration) and fascin (0.5 μM final concentration) into these droplets.

For the release of F-actin-containing GUVs a lipid composition of DOPC:cholesterol:DOPG (76 mol% DOPC, 20 mol% cholesterol, 3 mol% DOPG including 1 mol% RhB-labelled DOPE) was used when creating the dsGUVs.

Microtubule formation within dsGUVs. Tubulin (kindly provided by Surrey's group, the Francis Crick Institute) was purified from pig brain according to previously described protocols[49]. It was then labelled with ATTO 488-SE (Life Technologies) as described earlier[50]. Tubulin concentrations were measured using UV spectroscopy ($\varepsilon_{280} = 115{,}000\ M^{-1}cm^{-1}$). The labelling ratio of ATTO 488-labelled tubulin was 0.65 dye molecules per tubulin dimer. Labelled and unlabelled tubulin were stored at −80 °C in PIPES storage buffer (20 mM PIPES pH 6.8, 7.25 mM $MgCl_2$, 1 mM EGTA, 1 mM 2-mercaptoethanol, 50 mM KCl, 31 mM glucose, 1 mg ml^{-1} glucose oxidase and 0.5 mg ml^{-1} catalase and 0.25 mg ml^{-1} beta-casein). To form microtubule networks inside the dsGUVs, two methods were tested:

Premixed approach: Tubulin 14.5 μM (10% labelled with ATTO 488-SE) dissolved in polymerization buffer (20 mM PIPES pH 6.8, 7.25 mM $MgCl_2$, 1 mM EGTA, 3 mM GTP, 1 mM 2-mercaptoethanol, 50 mM KCl, 31 mM glucose, 1 mg ml^{-1} glucose oxidase and 0.5 mg ml^{-1} catalase, 0.25 mg ml^{-1} beta-casein) was mixed with the LUV solution (90% DOPC, 9% DOPS and 1% RhB-DOPE) and introduced into the microfluidic device via an aqueous channel. To avoid tubulin polymerization prior to droplet formation, droplets were produced at 4 °C. After droplet production, tubulin polymerization was triggered by transferring the droplets to a 37 °C observation chamber.

Pico-injection approach: Two experimental steps were required for producing stable microtubules in dsGUVs. The first step entailed the creation of dsGUVs (90% DOPC, 9% DOPS and 1% RhB-DOPE) that contain tubulin polymerization buffer. The second step was the pico-injection of the storage buffer containing tubulin (14.5 μM) into these droplets to get a 10 μM final concentration.

Bulk release approach. For the successful release of integrin $\alpha_{IIb}\beta_3$- or F-actin-containing GUVs (Fig. 4a,b, respectively), the lipid compositions of the dsGUVs were optimized in each case. More details are given in the corresponding methods.

Following the formation of protein-containing dsGUVs, 100 μl oil/dsGUV-containing solution was transferred into a 2 ml Eppendorf tube containing 1 ml FC-40 oil/surfactant solution (identical to the FC-40 oil/surfactant solution used for dsGUV production). Next, 100 μl of the appropriate buffer (actin polymerization buffer or integrin activation buffer) was pipetted on to the droplet emulsion. To destabilize the polymer shell of the droplets, 100 μl of 20 vol% perfluoro-1-octanol destabilizing surfactants (Sigma-Aldrich) dissolved in FC-40 oil was added. The Eppendorf tube was carefully tilted and slowly rotated until the emulsion was broken. The released GUVs were studied in an observation chamber made of BSA-coated glass slides and cover slips. The observation chambers were prepared by incubating the glass with 10 mg ml^{-1} BSA in PBS for 2 h at room temperature, followed by two 5 min washing steps—one with PBS and one with water.

Code availability. Matlab 2015 SP1 codes used for FRAP and intensity analyses are available in the Supplementary Notes 5 and 6, respectively.

Data availability. Data supporting the findings of this study are available within the article and its Supplementary Information files and from the corresponding authors on reasonable request.

References

43. Niu, X., Gulati, S., Edel, J. B. & deMello, A. J. Pillar-induced droplet merging in microfluidic circuits. *Lab Chip* **8,** 1837–1841 (2008).
44. Eberhard, C. *Online-Ressource* (Heidelberg Univ., 2012).
45. Zimmermann, B., Diez, M., Zarrabi, N., Graber, P. & Borsch, M. Movements of the epsilon-subunit during catalysis and activation in single membrane-bound H+-ATP synthase. *EMBO J.* **24,** 2053–2063 (2005).
46. Heitkamp, T., Deckers-Hebestreit, G. & Borsch, M. in *Single Molecule Spectroscopy and Superresolution Imaging IX* Vol. 9714 (eds Enderlein, J., Gregor, I., Gryczynski, Z. K., Erdmann, R. & Koberling, F.) (Spie-Int Soc Optical Engineering, 2016).
47. Mashaghi, S. & van Oijen, A. M. External control of reactions in microdroplets. *Sci. Rep.* **5,** 11837 (2015).
48. Gan, B. S., Krump, E., Shrode, L. D. & Grinstein, S. Loading pyranine via purinergic receptors or hypotonic stress for measurement of cytosolic pH by imaging. *Am. J. Physiol.* **275,** C1158–C1166 (1998).
49. Castoldi, M. & Popov, A. V. Purification of brain tubulin through two cycles of polymerization-depolymerization in a high-molarity buffer. *Protein Expr. Purif.* **32,** 83–88 (2003).
50. Hyman, A. *et al*. Preparation of modified tubulins. *Methods Enzymol.* **196,** 478–485 (1991).

nature materials

SUPPLEMENTARY INFORMATION

DOI: 10.1038/NMAT5005

In the format provided by the authors and unedited.

Sequential bottom-up assembly of mechanically stabilized synthetic cells by microfluidics

Marian Weiss,[1,2‡] Johannes Patrick Frohnmayer,[1,2‡] Lucia Theresa Benk,[1,2‡] Barbara Haller,[1,2] Jan-Willi Janiesch,[1,2] Thomas Heitkamp,[3] Michael Börsch,[3] Rafael B. Lira,[4] Rumiana Dimova,[4] Reinhard Lipowsky,[4] Eberhard Bodenschatz,[5] Jean-Christophe Baret,[6,7] Tanja Vidakovic-Koch,[8] Kai Sundmacher,[8,9] Ilia Platzman,[1,2*] and Joachim P. Spatz[1,2*]

[1]*Department of Cellular Biophysics, Max Planck Institute for Medical Research, Jahnstraße 29, 69120 Heidelberg, Germany*

[2] *Department of Biophysical Chemistry, University of Heidelberg, Im Neuenheimer Feld 253, 69120 Heidelberg, Germany*

[3] *Single-Molecule Microscopy Group, Jena University Hospital, Friedrich Schiller University Jena, 07743 Jena, Germany*

[4]*Theory & Bio-Systems, Max Planck Institute of Colloids and Interfaces, 14424 Potsdam, Germany*

[5]*Laboratory for Fluid Dynamics, Pattern Formation and Biocomplexity, Max Planck Institute for Dynamics and Self-Organization, 37077 Göttingen, Germany*

[6]*Droplets, Membranes and Interfaces, Max Planck Institute for Dynamics and Self-Organization, 37077 Göttingen, Germany*

[7]*Soft Micro Systems, CNRS, Univ. Bordeaux, CRPP, UPR 8641, 115 Avenue Schweitzer, 33600 Pessac, France*

[8]*Process System Engineering, Max Planck Institute for Dynamics of Complex Technical Systems, 39106 Magdeburg, Germany*

[9]*Otto-von-Guericke University Magdeburg, Process Systems Engineering, Universitätsplatz 2, 39106 Magdeburg, Germany*

Corresponding authors:
ilia.platzman@mpimf-heidelberg.mpg.de and joachim.spatz@mpimf-heidelberg.mpg.de

Supplementary Text

Supplementary Movie Legends

Supplementary Movie 1

The formation of a dsGUV out of the encapsulated GUVs.
Representative time-lapse fluorescence microscopy of the process showing the transformation of the encapsulated GUVs (ATTO 488-labeled DOPE) into a continuous supported lipid bilayer at the droplet inner interface. To transform the encapsulated GUVs into a supported lipid bilayer at the copolymer-stabilized droplet inner interface, 10 mM Mg^{2+} was applied during droplet production or by means of pico-injection.

Supplementary Movie 2

Microfluidic release device.

The video shows the dsGUVs encounter the aqueous phase in a wide perpendicular channel. To minimize the mechanical impact on the dsGUVs at the oil/water junction, the droplets were decelerated using passive trapping structures within the microfluidic channels (i.e., rows of pillars separated by distances smaller than the representative droplets dimensions), which we designed for the efficient release of GUVs.

Supplementary Movie 3

Pyranine as a pH sensor inside microfluidic droplets.

The video shows water-in-oil droplets immobilized in a microfluidic trapping device. The pH-sensitive fluorophore pyranine (concentration: 50µM) in ATP activity buffer was encapsulated into the droplets. To change the pH inside the droplets via the oil phase, acidic oil (containing 1µL of trifluoroacetic acid per 1 ml FC40 oil) and basic oil (containing 1µL of propyl amine per 1 ml FC40 oil) were alternately flushed through the device. As a result, the pH inside the droplets changed accordingly from acidic to basic and vice versa. The encapsulated fluorophore pyranine was simultaneously excited at 405nm and 458nm wavelength and the corresponding emission signal was recorded. Dominant 405nm detection signal indicated by blue color corresponds to basic pH, dominant 458nm detection signal indicated by green color corresponds to acidic pH.

Supplementary Methods

Preparation of large unilamellar vesicles (LUVs) and free-standing giant unilamellar vesicles (GUVs).
Lipids used in this study: 1,2-dioleoyl-sn-glycero-3-phosphocholine (DOPC), 1,2-dioleoyl-sn-glycero-3-phosphoethanolamine (DOPE), 1,2-dioleoyl-sn-glycero-3-phospho-L-serine (DOPS), 1,2-dioleoyl-sn-glycero-3-[(N-(5-amino-1-carboxypentyl)iminodiacetic acid) succinyl] (DGS-NTA), 1,2-dioleoyl-sn-glycero-3-phosphoethanolamine-N-(lissamine rhodamine B sulfonyl) (RhB DOPE), 1-palmitoyl-2-hydroxy-sn-glycero-3-phosphate (Phosphatidic acid), L-α-phosphatidylcholine (Egg PC), L-α-phosphatidylglycerol (Egg PG) were purchased from Avanti (Avanti Polar Lipids, USA) and used without further purification. ATTO 488 1,2-dioleoyl-sn-glycero-3-phosphoethanolamine was purchased from ATTO TEC (Siegen, Germany);
To obtain the formation of dsGUVs, solutions of LUVs or GUVs, consisting of different lipid compositions, were generated according to previously reported protocols.[1, 2] In brief, lipids were dissolved in pure chloroform, mixed at desired composition and concentration and dried

under a gentle stream of nitrogen. To remove traces of the solvent, lipids were kept under vacuum in desiccator for roughly 1 h. Dried lipids were then resuspended by addition of the desired buffer, followed by one hour of vortexing. LUV size was homogenized by extruding the solution 7 times through a polycarbonate filter (Whatman, Germany) with a pore size of 50 nm using an extruder (Avanti Polar Lipids, USA). The mean LUV diameter distribution was determined to be 100 ±10 nm using DLS. Solutions containing LUVs were stored at 4°C for not longer than 48 h or used immediately after production.
GUVs consisting of DOPC:DOPE:DOPS 8:1:1, including 1% ATTO 488-labeled DOPE were formed using the electroformation protocols as described previously.[2] In brief, lipid mixtures at the desired concentration (from 1 to 5 mM) were dissolved in pure chloroform and spread onto two indium tin oxide (ITO) coated glasses (Sigma-Aldrich, Germany). Following chloroform evaporation, the electroformation cell was assembled. Towards this end, the two ITO coated glasses were faced to each other with the conductive sides. To avoid direct contact two Teflon spacers (1 mm) were used. Copper tape (3M, USA) was used to connect the conducting sides with a signal generator (RS Components, Germany). Subsequently, the chamber was filled with Milli-Q water (Millipore filtered) and sealed with two-component glue (Twinsil Picodent GmbH, Germany). An alternating electrical potential of 10 Hz at 1 V amplitude was applied for 2 h to form GUVs. Finally the GUVs were collected using a syringe. Following vesicles production, the solutions were used immediately for encapsulation into microfluidic water-in-oil copolymer-stabilized droplets.

Block copolymer surfactant synthesis. Three types of block-copolymer surfactants were synthesized according to protocols reported earlier [3, 4] and used to produce droplets: Two triblock-copolymers PFPE(7000 g/mol)-PEG(1400 g/mol)-PFPE(7000 g/mol) (TRI7000) and PFPE(2500 g/mol)-PEG(600 g/mol)-PFPE(2500 g/mol) (TRI2500) and a gold-linked diblock-copolymer surfactant Au-PEG(436 g/mol)-PFPE(7000 g/mol). Following synthesis, triblock surfactants were mixed separately with gold-linked surfactants and dissolved in FC-40 fluorinated oil (3M, USA) to the final concentrations of 2.5 mM and 3 μM for triblock and gold-linked surfactants, respectively. NOTE: The two types of triblock copolymer surfactants (i.e. TRI7000 and TRI2500) mixed with gold-linked surfactants were tested and compared in all experiments. If not stated otherwise, the same results were observed.

Droplet-based microfluidics. Droplet-based microfluidic devices made of PDMS (Sylgard 184, Dow Corning, USA) were prepared by photo- and soft-lithography methods[5, 6] as described previously.[3] To control the droplet diameter during their creation, two different nozzle designs at the flow-focusing junction were implemented (Supplementary Figures 4 A and B). Syringe pumps PUMP 11 ELITE (Harvard apparatus, USA) were used to control flow rates of 120 μL/h for the aqueous phase and 160 μL/h for the oil phase as required for stable droplet creation (diameter d = 40 μm) at the rate of 1 kHz. In case of big droplets (d = 100 μm) the flow rates were adjusted to 650 and 850 μL/h for aqueous and oil phases, respectively to achieve a stable droplet creation at a rate of 1 kHz.
Due to the variety of required cellular components in the droplets the microfluidic device was integrated with small and compact electrodes to apply an electric potential. Electrical fields allow destabilization (poration) of surfactants and lipid bilayers towards controlled injection (pico-injection) of different cellular components into the droplets. The design of the droplet-based pico-injection unit was adapted from Abate et al.[7] Droplets were introduced into the device using a MFCS-EZ flow control system (Fluigent, France). The spacing between the droplets was controlled through addition of oil via the second oil channel (Supplementary Figure 4F). Following separation step, isolated droplets passed an alternating electrical field (frequency 1kHz, potential 250 V) generated by HM 8150 signal generator (HAMEG, Germany) and amplified by 623B-H-CE amplifier (TREK, USA) and two electrodes made of

Indalloy 19 (51% indium, 32.5% bismuth, 16.5% tin, GPS Technologies, Germany). This process destabilizes the droplet copolymer shell and lipid bilayer and allows introduction of bio-reagents via a pressurized injection channel (Supplementary Figure 4G). The injection volume can be ranged between 1 to 100 pl, dependent on the applied pressure.
For analysis, droplets were collected and transferred to the observation chamber (Supplementary Figure 5). The chamber was made of two single or sandwiched stripes of double face sticky tapes (Tesa, Germany. Thickness ≈ 80 µm or 160 µm for analysis of small and large droplets, respectively) as spacers, glued between two cover slips (Carl Roth, Germany). Finally, the chamber was filled with surfactant-containing oil and closed by two-component glue (Twinsil, Picodent GmbH, Germany).

Glass coatings for integrin-reconstituted GUVs adhesion experiments. To validate the biological functionality of the reconstituted integrin after the process of release, the adhesion of the integrin-reconstituted GUVs to fibrinogen-, fibronectin-, collagen-, and BSA-coated glass surfaces was examined and compared (Supplementary Figure 8). Therefore, dsGUVs with reconstituted $\alpha_{IIb}\beta_3$ integrin were formed and released as described in (Online Methods). For adhesion experiments integrin activation buffer (20 mM TRIS/HCl, pH 7.4, 50 mM NaCl, 0.5 mM $CaCl_2$, 1 mM $MnCl_2$ and 1 mM $MgCl_2$) was used inside and outside the GUVs. Following release the integrin-reconstituted GUVs were transferred to an observation chamber (Supplementary Figure 5) containing fibrinogen-, fibronectin-, collagen-, or BSA-coated glass slides. The adhesion was analyzed after 8 h incubation at 4°C to allow the integrin to interact with the different coatings. For these experiments fibronectin isolated from human plasma[8] was dissolved in PBS, collagen Type I (calf skin, Sigma-Aldrich, Germany) was dissolved in 0.1 M acetic acid and fibrinogen (human plasma, Merck Millipore, Germany) was first dissolved in 8.5% NaCl and for the incubation transferred to PBS.
For coating the glass surface of the observation chamber, pretreated glass slides (O_2 plasma, 200 W, 30 s) were incubated with 0.1 mg/ml protein solution (8.5 µg/cm^2) over night at 4°C (fibrinogen and collagen) or 1.5 h at room temperature (fibronectin). For the BSA coating the glasses were incubated with 10 mg/ml BSA in PBS for 2 h at room temperature, followed by a washing step with PBS and water for each 5 min. After incubation, the glass slides were air dried over night at 4°C. The coverslips for the observation chamber were passivated with BSA.

Microscopy. All experiments were performed on a Leica SP5 confocal microscope (Leica Microsystems, Germany) equipped with an argon and a white light laser. The measurements were conducted at 25°C and in case of microtubule analysis at 37°C. Droplets, sealed in an analysis chamber, were observed via a 63x oil objective (HCX PL APO 63x/1.40-0.60; Leica Microsystems GmbH, Germany). Fluorophores were exited at 488, 550 and 555 nm and the detection windows were set at 498-540 and 560-620 nm and 565-625 nm in case of ATTO 488, Rhodamine B and TAMRA-labeling, respectively. The pinhole for data acquisition was set to 1 Airy unit, which corresponds to an Airy disk diameter of 96 µm and 0.9 µm thickness of the optical slice.

FRAP measurements. Due to the density differences between the aqueous droplets and the surrounding oil (1.0×10^3 vs. 1.9×10^3 kgm^{-3}), the droplets ascend towards the upper slide of the observation chamber (Supplementary Figure 5). In this position, the droplets were scanned in z-direction until the bottom slice of the droplet was identified. The base of the droplet was chosen as a focal plane for FRAP measurements in order to exclude any influence from the cover slip at the chamber ceiling. A circular spot with a diameter of 5 µm was selected as the bleaching area. It should be noted that in case of FRAP measurements performed inside the droplets or on their periphery the actual bleaching area was measured and corrected for each measurement due to distortion of the optical path as a reason of diffraction/refraction at the

oil/water interface. Time course of each FRAP experiment included 10 pre-bleaching images, 2 to 10 bleach cycles to eliminate the fluorescent signal and 50 to 200 post-bleaching images to record the fluorescence recovery. The bleaching time was adjusted to each fluorophore and laser used in the experiments, the acquisition frequency of post-bleaching images was adapted to the total recovery time. The average diffusion coefficient for each experiment and its standard error were calculated from at least 20 measurements. The analysis followed the protocols proposed by Axelrod et al.[9] and Soumpasis[10] as described in Supplementary Note 3.

Raman spectroscopy. For Raman spectra collection released GUVs or dsGUVs were injected into the observation chamber (Supplementary Figure 5). GUVs or dsGUVs, sealed in an analysis chamber, were observed via a 100x oil objective (NA 1.2, Zeiss, Germany) using a confocal Raman microscope (Alpha300RA, WITec GmbH, Germany). To collect Raman scattered light, the same objective was used for focusing a 532 nm laser (20 mW, spot size 350 nm) onto single GUVs or dsGUVs. The acquisition time was fixed to 2.14 seconds with five accumulations for each collection window. At the end of spectra collection the location of the observed subject was investigated and, in case the location was preserved the collected data was saved. The representative Raman spectra of the dsGUVs and of the released GUVs can be observed in Supplementary Figure 7.

Fluctuation analysis. Fluctuation analysis was performed following the protocol described earlier.[11] The GUVs were placed in a chamber made of two cover slips and a 2 mm-thick ring made of Teflon, and observed under phase contrast. The data was acquired at room temperature ~23°C. The acquisition of five thousands of snapshots was done by high-resolution camera (pco.edge, PCO AG, Kelheim, Germany). More than 10 vesicles per type of sample were examined.
The bending rigidity of vesicles released from droplets was measured and compared to that of vesicles prepared following the method of electrofromation[12, 13] or gel-assisted swelling.[14] The membrane composition was DOPC:POPC:Chol (4:4:2) in mole ratios and small amount of the ATTO 488 labeled DOPE was also added at concentration of 1 mol% of total lipid. The buffer composition used for fluctuation analysis of the released GUVs was adjusted to be similar to integrin activation buffer within the GUVs (20 mM TRIS/HCl, pH 7.4, 50 mM NaCl, 0.5 mM $CaCl_2$, 1 mM $MnCl_2$ and 1 mM $MgCl_2$). The bending rigidity of the released vesicles was measured to be 21.5 ± 3.4 k_BT (standard deviation). This value lies in the range of typical values reported for the bending rigidity of PC membranes,[15] suggesting that the bilayers are clean of impurities. The methods of electroformation and gel-assisted swelling did not yield suitable vesicles (the vesicles were small and with defects or multilamellar) when grown in the buffer used for the preparation of dsGUVs. Therefore, we electroformed vesicles with the same membrane composition but in solution of 1 mM $MgCl_2$. The bending rigidity values for these membranes were found to be 25.3 ± 3.0 k_BT ideally corresponding to the data for released vesicles.

Supplementary Notes

Supplementary Note1. Calculation of minimal lipid concentration required to form a continuous lipid bilayer inside droplets - dsGUV:

The following lipid concentration calculation is done for droplets with 75 µm radius. The volume $V_{droplet}$ and the surface area $A_{droplet}$ of a spherical droplet is given by

$$V_{droplet} = \frac{4}{3}\pi r^3 = 1.8 \times 10^6\ \mu m^3 = \ 1.8\ nL$$

and

$$A_{droplet} = 4\pi r^2 = 7.1 \times 10^{10}\ nm^2.$$

Assumption: Average area occupied by a single phospholipid in a lipid membrane equals[16]

$$A_{headgroup} = 0.7\ nm^2.$$

The amount of lipids per droplet needed to form a complete lipid bilayer is therefore:

$$N_{lipids} = 2 * A_{droplet}/A_{headgroup} = 2.3 \times 10^{11}.$$

Thus, the lipid concentration required to form a lipid bilayer inside droplets is

$$c = \frac{N_{lipids}}{V_{droplet} * N_A} = \frac{6}{r \cdot N_A \cdot A_{headgroup}} = 190\ \mu M.$$

The concentration for droplets with different radii used in this study is c(r=50 µm) = 285 µM and c(r=20 µm) = 712 µM.

For the experiments an excess of ≈15% in lipid concentration was used for the following two reasons: 1) to compensate for possible lipids loss during the production; and 2) to compensate for volume increase due to pico-injection.

To validate experimentally the relevance of theoretically estimated lipid concentration, we systematically varied the amount of fluorescently-labeled lipids injected into monodisperse droplets and recorded their fluorescence intensity at the droplet interface. In case of minor lipid amount which would not cover the complete inner surface of the droplet we did not see the assembly of smaller GUVs than the size of the droplet itself. Instead we observed fusion of available lipids at the inner wall of the droplet. A plot of the measured data is shown in Supplementary Figure 1. Considering the diameter of 120µm of the droplets used in this experiment, a calculated concentration of 237 µM lipids is required for full bilayer coverage. As can be observed in Supplementary Figure 1, the intensity values are increasing approximately linear up to the theoretical estimated concentration. At elevated concentration the intensity reaches a plateau. It should be noted that at higher concentrations the excess lipids form aggregates of liposomes at the droplet interface. Inhomogeneous aggregation of liposomes on the droplet's periphery affecting precise estimation of the intensity. Therefore, higher deviation in the recorded intensity at 500µM is attributed to this effect.

Supplementary Note 2. Calculation of vesicle diffusion in microfluidic droplets

Assuming 3D Brownian motion, the mean square displacement $\langle r^2(t)\rangle$ of a particle in solution is

$$\langle r^2(t)\rangle = 6D\langle t\rangle.$$

The mean time $\langle t\rangle$ needed for the particle to travel the distance $\sqrt{\langle r^2(t)\rangle}$ is therefore

$$\langle t \rangle = \frac{\langle r^2(t) \rangle}{6D}.$$

The diffusion coefficient D of a spherical particle with radius R in a solution with viscosity η for a given temperature T is

$$D = \frac{k_B T}{6\pi\eta R}.$$

Therefore, the average time for a vesicle with radius R needed to diffuse from the center of the droplet to the periphery $\left(\sqrt{\langle r^2(t) \rangle} = 20\ \mu m\right)$ is

$$\langle t \rangle = \frac{\langle r^2(t) \rangle}{6} \frac{6\pi\eta R}{k_B T}.$$

Assuming an aqueous solution with $\eta = 0.1\ Pa \cdot s$ and a temperature$T = 25°C$, the average time for all vesicle to diffuse from the centrum to the periphery of the droplet with diameter 40 μm is

$$\langle t(R = 50\ nm) \rangle \approx 15\ s$$

and

$$\langle t(R = 5\ \mu m) \rangle \approx 25\ min.$$

Supplementary Note 3. Evaluation of FRAP data

The analysis followed a protocol proposed by Axelrod et al.[9] and Soumpasis.[10] To correct the background noise I_{bg}, the detector signal was measured in the oil phase using the same settings as for the FRAP measurements. I_{bg} was subsequently subtracted from all the measured intensity values. Average intensity values of the bleaching spot, I(t), and as a reference of the whole droplet base, T(t), were extracted from the recorded images. I(t) and T(t) were normalized by the averages of the prebleaching values, I_{pb} and T_{pb}. To correct for photofading the intensities of the bleached spot were multiplied with the reciprocal, normalized intensities of the droplet base, T(t). Thus the normalized and corrected intensities, I_{nor}, were calculated as

$$I_{nor} = \frac{I(t) - I_{bg}}{I_{pb} - I_{bg}} \frac{T_{pb} - I_{bg}}{T(t) - I_{bg}}.$$

A nonlinear least-square fit was then applied using MATLAB R2015a SP1 (Mathworks, USA) to fit an exponential function $f(t)$,

$$f(t) = a\big(1 - exp(\lambda \cdot t)\big),$$

to the normalized intensities, I_{nor}. The resulting values of the coefficient λ were then used to calculate the half-recovery time $\tau_{1/2}$ for each bleaching experiment,

$$\tau_{1/2} = \frac{-\log(0.5)}{\lambda}.$$

The diffusion coefficient, D, is related to the half-recovery time $\tau_{1/2}$ via the square radius of the bleaching spot, assuming Gaussian bleaching profile,

$$D = 0.32 \frac{r^2}{\tau_{1/2}}.$$

The average diffusion coefficient for each experiment and its standard error were calculated from at least 20 measurements (Supplementary Figure 9).

Supplementary Note 4. Calculation of number of integrin proteins that might be reconstituted in dsGUVs.

Droplet surface area:

$$S(r = 20\mu m) = 5026\ \mu m^2$$
$$S(r = 50\mu m) = 31416\ \mu m^2$$

Area of a lipid in a membrane (from literature)

$$A_{lip} \approx 0.7nm^2$$

Cross-section of the transmembrane domain of integrin (two α helices).[17]

$$A_{int} = 2nm^2$$

Integrin/Lipid Ratio	Surface area of lipid bilayer with one reconstituted integrin.	N_{int} $(r = 20\mu m)$	N_{int} $(r = 50\mu m)$
1:1000	$\frac{1000 * 0.7nm^2}{2} + 2nm = 352nm^2$	$1.43 * 10^7$	$8.92 * 10^7$
1:10,000	$\frac{10{,}000 * 0.7nm^2}{2} + 2nm = 3502nm^2$	$1.44 * 10^6$	$8.97 * 10^6$

Supplementary Note 5. Matlab code for FRAP analysis

```
%%%%%%%%%%%%%%%%%%%%%%%%%%%%%%%%%%%%%%%%%%%%%%%
%% FRAP evaluation
% version 5 20161010
% Matlab-script for the evaluation of FRAP data. This script is designed to to evaluate '.csv' files
exported
% using the Leica Microscopy Software. For correct evaluation the files should contain
% three columns, first the intensity values form the bleaching spot, second a reference spot
% and a thrid a larger area containing the bleaching spot. The data sets can differ in time steps
and total
% number of datapoints. The script will output the computed diffusion coefficient for each dataset
as well
% the average diffusion coefficient and it's corresponding standard error. Optionally the script
will draw
% graphs of each evaluation step.

%Program timer
%tic

%%%%%%%%%%%%%%%%%%%%%%%%%%%%%%%%%%%%%%%%%%%%%%%
%% A set of parameters that control the evaluation of the results
% Plotting switch. If value is true all intermediary results are plotted into
% pdf files. This slows down script drastically
plotall = true ;
% Radius of the bleached spot in Âµm. Important for the evaluation of the
% diffusion coefficient
w = 2.5;
% For good results its important, to correct the collected data points for background.
bg=0;
% The calculation is on standard done according to protocols published by Axelrod et al. (1976) and
Soumpasis (1983).
% Alternatively a model proposed by Kang et al. (2012) can be used, correcting for diffusion during
the bleaching.
% To derive the prefactor the script 'Frap radius evaluation.m' can be used.
pf=0.32;

%%%%%%%%%%%%%%%%%%%%%%%%%%%%%%%%%%%%%%%%%%%%%%%
%% Main body of code
%%%%%%%%%%%%%%%%%%%%%%%%%%%%%%%%%%%%%%%%%%%%%%%

%%%%%%%%%%%%%%%%%%%%%%%%%%%%%%%%%%%%%%%%%%%%%%%
```

```
%% Importing the data and removing rows with empty cells
files = dir('*.csv');
for i=1:length(files)
    data=importdata(files(i).name);
    J=all(~isnan(data.data),2);
    A{i}=data.data(J,:);
    clear data J
end

%%%%%%%%%%%%%%%%%%%%%%%%%%%%%%%%%%%%%%%%%%%%
%% Plotting of raw data
if plotall == true
for i=1:length(files)
   figure('vis', 'off');
    plot1=plot(A{i}(:,1),A{i}(:,2:4),'LineStyle','none');
    set(plot1(1),'Marker','o','DisplayName','ROI1');
    set(plot1(2),'Marker','.','DisplayName','ROI2');
    set(plot1(3),'Marker','x','DisplayName','ROI3');
    xlabel('time [s]');
    ylabel('intensity');
    title(files(i).name)
    print(sprintf('raw%02d',i) ,'-dpdf')
end
end

%%%%%%%%%%%%%%%%%%%%%%%%%%%%%%%%%%%%%%%%%%%%
%% Data correction and normalization
% Each dataset is corrected for background, normalized by the prebleaching value
% and corrected for photofading in this step
for i=1:length(files)
    B{i}=zeros(length(A{i}),2);
    %% Mean intensity of focus point before bleach
    Ipre=mean(A{i}(1:10,2));
    %% Mean intensity of the total cell before bleach
    Tpre=mean(A{i}(1:10,4));
    %% Calculating normalized values (without background substration)
    B{i}(:,1)=A{i}(:,1);
    B{i}(:,2)=(A{i}(:,2)-bg)./(Ipre-bg) * (Tpre-bg) ./ (A{i}(:,4)-bg);
end

clear i j A Ipre Tpre bg

%%%%%%%%%%%%%%%%%%%%%%%%%%%%%%%%%%%%%%%%%%%%
%% Plotting normalized graphs
if plotall == true
for i=1:length(files)
   figure('vis', 'off');
    plot(B{i}(:,1),B{i}(:,2),'Marker','o','LineStyle','none','DisplayName','B(:,1.6)');
    xlabel('time [s]');
    ylabel('intensity');
    title(files(i).name)
    print(sprintf('normalized%02d',i) ,'-dpdf')
end
clear i
end

%%%%%%%%%%%%%%%%%%%%%%%%%%%%%%%%%%%%%%%%%%%%
%% Initialization of the fitting model
% As fitting function an exponential recovery curve is chosen. A robust, non-linear least square has
proven to
% show good results. The fit outputs information about the fit quality to allow debugging.
    fo = fitoptions('method','NonlinearLeastSquares','Lower',[0 0],'Upper',[1 Inf],
'Robust','Bisquare');
    st = [1 1]; %starting point
    set(fo,'Startpoint',st);
    ft = fittype('a*(1-exp(-t*b))',...
               'dependent',{'y'},'independent',{'t'},...
               'coefficients',{'a','b'});

%%%%%%%%%%%%%%%%%%%%%%%%%%%%%%%%%%%%%%%%%%%%
%% The normalized data is fitted to the previously initialized fitting model. The results are
directly plotted.
C=zeros(2,length(files));
for i=1:length(files)
    [cf,gof] = fit(B{i}(11:length(B{i}),1)-B{i}(11,1),B{i}(11:length(B{i}),2)-B{i}(11,2),ft,fo);
    C(:,i) =  transpose(coeffvalues(cf));
    if plotall == true
        figure('vis', 'off')
        hold on
        ylim([-0.05 0.2])
        plot(B{i}(:,1)-B{i}(11,1),B{i}(:,2)-
B{i}(11,2),'Marker','o','LineStyle','none','DisplayName','B(:,1.6)');
        plot(cf);
        xlabel('time [sec]','FontSize',20)
        ylabel('normalized fluorescence Intensity','FontSize',20)
        title(files(i).name)
        print(sprintf('fitted%02d',i) ,'-dpdf')
    end
    clear cf gof
end

clear i st fo ft plotall B

%%%%%%%%%%%%%%%%%%%%%%%%%%%%%%%%%%%%%%%%%%%%
```

```
%% Calculation of diffusion coefficients
% The values are computed from the fitting results and the size of the bleaching spot. They are
% first calculated for each dataset seperately and then the average and standard error is computed.
% The calculation is on standard done according to protocols published by Axelrod et al. (1976) and
Soumpasis (1983).
% Alternatively a model proposed by Kang et al. (2012) can be used, correcting for diffusion during
the bleaching
tauh=-log(0.5)./C(2,:);
C(3,:) = pf*w^2./tauh;
D = [mean(C(3,:)), std(C(3,:))/sqrt(length(C(3,:)))];

%%%%%%%%%%%%%%%%%%%%%%%%%%%%%%%%%%%%%%%%%%%%%
%% Saving the results
save coefficients.txt C -ASCII
fid = fopen('diffusion_coefficient.txt', 'w');
fprintf(fid, 'diffusion_coefficient std_error [ÂµM^2/s]\n');
fprintf(fid, '%f    %f',D);
close

clear files w fid tauh pf

%toc
```

Supplementary Note 6. Matlab code for fluorescence intensity analysis

```
%%%%%%%%%%%%%%%%%%%%%%%%%%%%%%%%%%%%%%%%%%%%%
%% Droplet intensity profile evaluation script
% version 4 20161205
% As there is refraction and defraction on the water oil interface of the droplets,
% it is difficult to compare the fluorescence intensity of GUV and dsGUV. This script
% tries to solve this problem by fitting and integrating the fluorescence
% intensity profile. This script is designed to to evaluate '.csv' files exported
% using the Leica Microscopy Software

%%%%%%%%%%%%%%%%%%%%%%%%%%%%%%%%%%%%%%%%%%%%%
%% A set of parameters that control the evaluation of the results
% Plotting switch. If value is true all intermediary results are plotted into
% pdf files. This slows down script drastically
plotall = true;


%%%%%%%%%%%%%%%%%%%%%%%%%%%%%%%%%%%%%%%%%%%%%
%% Main body of code
%%%%%%%%%%%%%%%%%%%%%%%%%%%%%%%%%%%%%%%%%%%%%

%%%%%%%%%%%%%%%%%%%%%%%%%%%%%%%%%%%%%%%%%%%%%
%% Importing the data and removing rows with empty cells
files = dir('*.csv');
for i=1:length(files)
    data=importdata(files(i).name);
    J=all(~isnan(data.data),2);
    A{i}=data.data(J,:);
    clear data J
end

%%%%%%%%%%%%%%%%%%%%%%%%%%%%%%%%%%%%%%%%%%%%%
%% Plotting of raw data
if plotall == true
  for i=1:length(files)
    figure('vis', 'off');
    hold on
    plot1=plot(A{i}(:,3),A{i}(:,4));
    set(plot1(1),'Marker','o','DisplayName','ROI1');
    xlabel('position [Âµm]');
    ylabel('intensity');
    title(files(i).name,'FontSize',24)
    print(sprintf('raw%02d',i) ,'-dpdf')
   end
end

%%%%%%%%%%%%%%%%%%%%%%%%%%%%%%%%%%%%%%%%%%%%%
%% Fitting of Gaussian functions to the peaks
% The data is split in two arrays around each peak and fitted with Gaussian functions
B=zeros(length(files)*2,2);

%%%%%%%%%%%%%%%%%%%%%%%%%%%%%%%%%%%%%%%%%%%%%
%% Finding good starting points
% Searches for the position and values of two intensity peaks of a droplet crossection.
for i=1:length(files)
    j=round(length(A{i})/2);
    [m1 p1]=max(A{i}(1:j,4));
    [m2 p2]=max(A{i}(j:length(A{i}),4));
    B(i*2-1,1)=m1;
    B(i*2,1)=m2;
%%%%%%%%%%%%%%%%%%%%%%%%%%%%%%%%%%%%%%%%%%%%%
%% Fitting a Gaussian function to the data via a nonlinear least square to the 'left' peak
% The fit uses the previously derived values as starting points
    fo = fitoptions('method','NonlinearLeastSquares','Lower',[0 0 0 2],'Upper',[100 A{i}(j,3) 1e-4
3], 'Robust','Bisquare');
    st = [m1 A{i}(p1,3) 1e-6 2.2]; %starting point
    set(fo,'Startpoint',st);
```

```
    ft = fittype('a1*exp(-((x-b1)/c1)^2) +c3',...
                 'dependent',{'y'},'independent',{'x'},'coefficients',{'a1','b1','c1','c3'});
    x=A{i}(1:j,3);
    y=A{i}(1:j,4);
    f1=fit(x,y,ft,fo);
    c=coeffvalues(f1);
    B(i*2-1,2)=c(1)*c(3)*pi^.5;
    clear c
%%%%%%%%%%%%%%%%%%%%%%%%%%%%%%%%%%%%%%%%%%%%%%%%
%% Fitting a Gaussian function to the data via a nonlinear least square to the 'right' peak
% The fit uses the previously derived values as starting points
    fo = fitoptions('method','NonlinearLeastSquares','Lower',[0 A{i}(j,3) 1e-10 2],'Upper',[100
A{i}(length(A{i}),3) 1e-4 3], 'Robust','Bisquare');
    st = [m2 A{i}(p2+j,3) 1e-6 2.2];
    set(fo,'Startpoint',st);
    x=A{i}(j:length(A{i}),3);
    y=A{i}(j:length(A{i}),4);
    f2=fit(x,y,ft,fo);
    c=coeffvalues(f2);
    B(i*2,2)=c(1)*c(3)*pi^.5;
    clear c
%%%%%%%%%%%%%%%%%%%%%%%%%%%%%%%%%%%%%%%%%%%%%%%%
%% Plotting of data with fitting results
        if plotall == true
          figure('vis', 'off');
          hold on
          plot(A{i}(:,3),A{i}(:,4));
          plot(f1);
          plot(f2);
          xlabel('position [µm]','FontSize',20)
          ylabel('Intensity','FontSize',20)
          title(files(i).name,'FontSize',24)
          print(sprintf('fitted%02d',i) ,'-dpdf')
    end
    clear x y j m1 m2 p1 p2 fo ft f1 f2 i st c
end
%%%%%%%%%%%%%%%%%%%%%%%%%%%%%%%%%%%%%%%%%%%%%%%%
%% Calculation of maximal intesity values and integrated intensity
% The columns contain in order: the mean maximal values, the corresponding standard error,
% the integrated intensity, and the corresponding standard error.
C(1,1)=mean(B(:,1));
C(1,2)=std(B(:,1))%/sqrt(length(files));
C(1,3)=mean(B(:,2))*10^6;
C(1,4)=std(B(:,2))*10^6%/sqrt(length(files));

%%%%%%%%%%%%%%%%%%%%%%%%%%%%%%%%%%%%%%%%%%%%%%%%
%% Saving the results
fid = fopen('intensitiy_values.txt', 'w');
fprintf(fid, 'max intensity [au] std error [au] integrated intensity [au*µm]  std error
[au*µm]\n %f  %f  %f  %f',C);
close

clear plotall files ans plot1 fid
```

Supplementary Figures

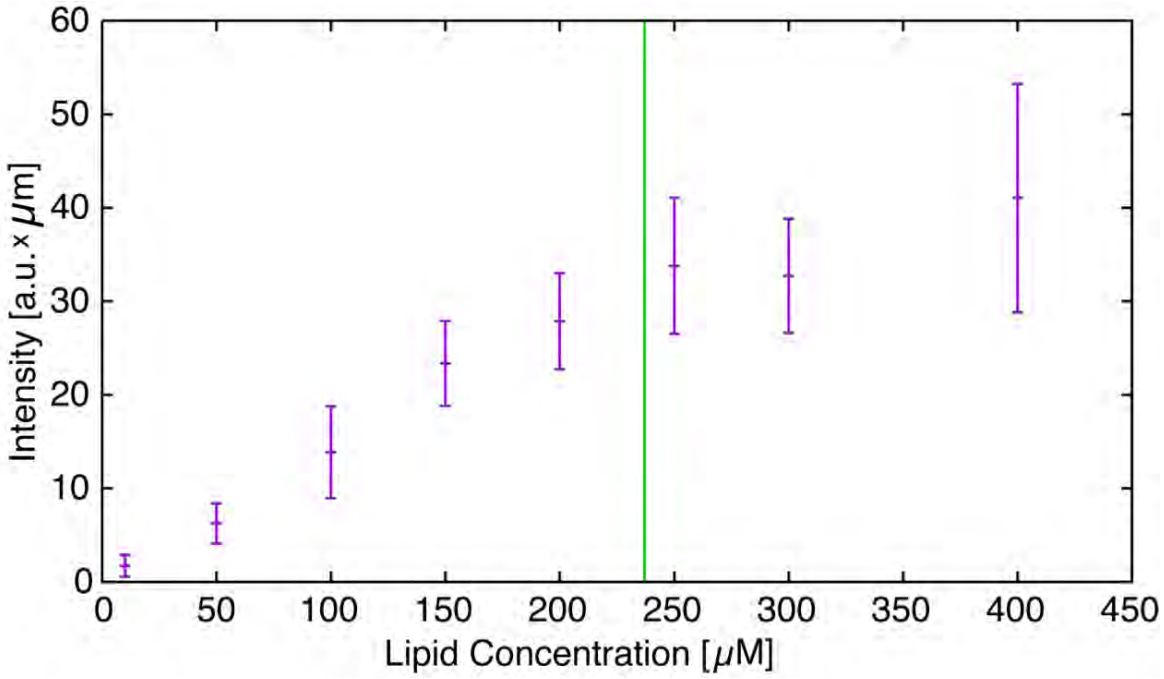

Supplementary Figure 1
Fluorescence intensity of the lipids at the droplets interface as a function of encapsulated lipid concentration.

To validate experimentally the relevance of theoretically estimated lipid concentration (237 μM, Supplementary Note 1), we systematically varied the amount of fluorescently-labeled lipids (egg PC:egg PG, 9:1, including 0. 5 % ATTO 488-labelled DOPE) encapsulated into 120 μm diameter monodisperse droplets and recorded their fluorescence intensity at the droplet interface. In case of lipid concentration lower than 237 μM no smaller GUVs than the size of the droplet itself were observed. Instead fusion of available lipids at the inner wall of the droplet was detected. As can be observed, the lipid fluorescence intensity values are increasing approximately linear up to the theoretical estimated concentration. At higher lipid concentration the intensity reaches a plateau. It should be noted that at higher concentrations the excess lipids form aggregates of liposomes at the droplet interface. Inhomogeneous aggregation of liposomes on the droplet's periphery affecting precise estimation of the intensity. Therefore, higher deviation in the recorded intensity at 400μM lipid concentration is attributed to this effect. The mean integrated intensity values and their standard deviation, indicated by the error bars, were derived from intensity profiles taken from twenty individual droplets, each intersecting the membrane twice rectangularly.

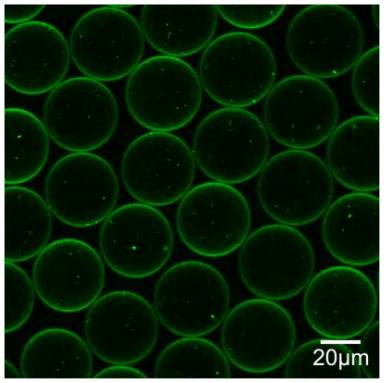

Supplementary Figure 2
Partial vesicle fusion due to 10 mM Ca^{2+} ions addition.

Representative fluorescence image of lipid distribution (DOPC:DOPE:DOPS 8:1:1, including 1% ATTO 488-labeled DOPE) within microfluidic water-in-oil droplets, containing 10 mM Ca^{2+} ions ($CaCl_2$), measured 1 h after creation.

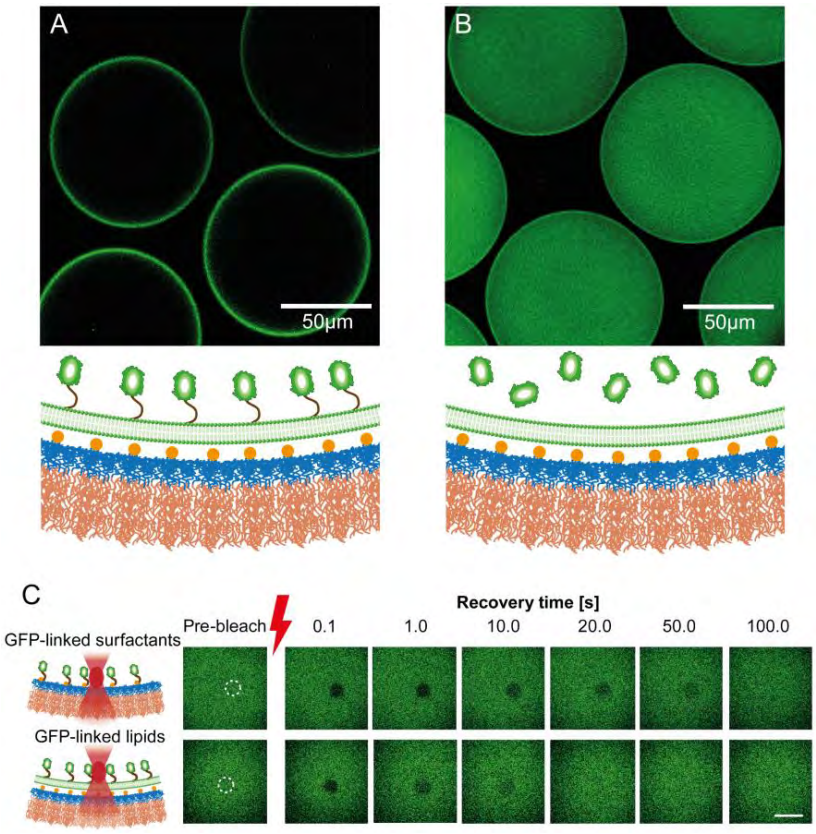

Supplementary Figure 3
Biofunctionalization of dsGUVs via DGS-NTA(Ni)lipids.

In order to test the functionalization of dsGUVs, (His6)-GFP was pico-injected into droplets. (A) For droplets containing DOPC:DGS-NTA(Ni), 9:1 (220 µM), (His6)-GFP was linked to the dsGUVs at the droplets periphery. (B) An equally distributed fluorescence signal was observed when no anchoring points were present (here: dsGUVs consisting of DOPC lipids only). (C) Representative FRAP experiments on the mobility of (His6)-GFP immobilized to the

copolymer-stabilized droplet interface (upper trace) or the dsGUV (lower trace). The bleached area is encircled in the pre-bleach frame and the recovery time (seconds after bleaching) is indicated on top of the fluorescence recovery frames. Scale bar 10 µm.

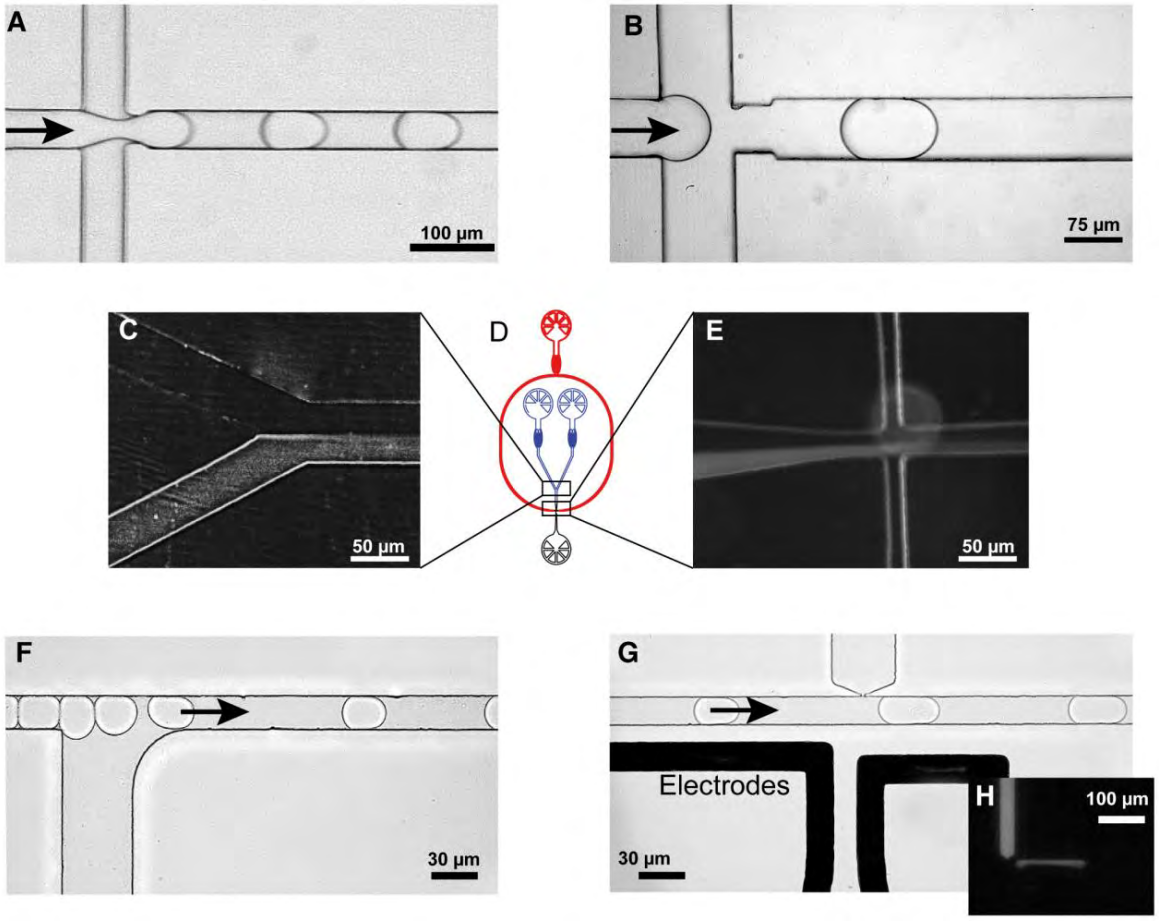

Supplementary Figure 4
Droplet-based microfluidic functional units.

Presentation of different droplet-based microfluidic operating units used in this research. (A) and (B) show representative images of the flow-focusing junctions for droplets production with a diameter of 40 and 100 µm, respectively. (D) shows a microfluidic droplet production device with two aqueous inlet channels (blue) and one oil channel (red). This device was implemented in actin-related experiments in order to avoid actin polymerization prior to droplet formation. Inset (C) and (E) show representative fluorescence images of the two phases for actin polymerization within the droplets. Bright phases represent the actin solution containing Alexa 488-labeled G-actin. The second phase contains all necessary bio-molecules for polymerization and bundling of actin. The solutions have a contact time in the millisecond range before getting encapsulated. Images (F) and (G) represent the pico-injection device for controlled introduction of different cellular components into droplets. (F) The spacing between the droplets carrying different biologically-active molecules is controlled through addition of oil via the second oil channel. (G) An alternating electric potential (1 kHz and 250 V) reduces the stability (poration) of the surfactants-lipid layer at the droplet interface for an aqueous injection of reagents from a pico-injection channel (injection volume can be ranged between 2 to 100 pl, dependent on the applied pressure). The injection process can be visualized by injection of ATTO 488-labeled F_0F_1-ATP synthase (H), using fluorescence microscopy.

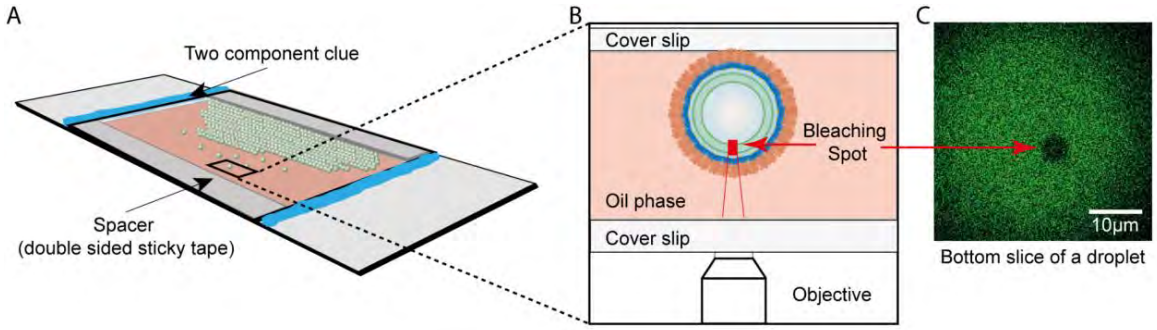

Supplementary Figure 5
Observation chamber and analysis setup.

(A) Shows the design of an observation chamber for droplet analysis. (B) Magnified cross-section representation of the analysis chamber. Due to the density differences, droplets rise to the top of the chamber. Confocal microscopy was used to scan the droplet in order to find the bottom plane. The lowest slice of the droplet was chosen as a focal plane for FRAP measurements in order to exclude any influence of stiff objects like in the case of the coverslip and the upper parts of the droplet. (C) Example of a FRAP experiment performed on dsGUV containing GFP-linked DGS lipids. The image shows a circular bleached spot with a 5 µm diameter.

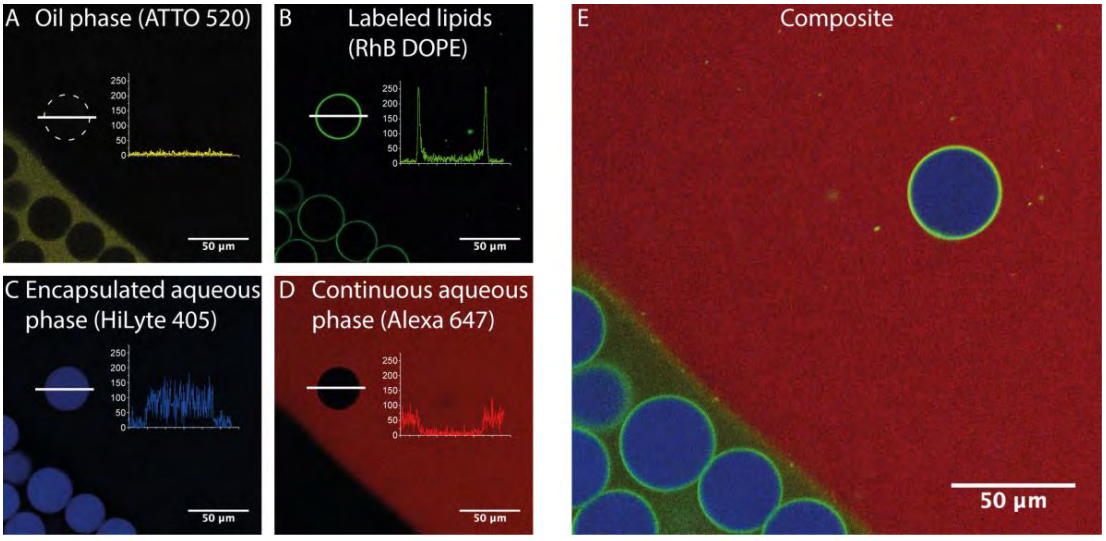

Supplementary Figure 6
Release of dsGUVs, preservation of content and checking for oil residues.

To evaluate if the lipid bilayer stayed intact during the release process the (A) oil phase (ATTO 520, yellow), the (B) lipid bilayer (RhB DOPE, green), the (C) encapsulated (HyLite 405, blue) and (D) continuous water phase (Alexa 647, red) were labeled with distinctive fluorophores. (E) A composite image of all channels. On the bottom left of each frame is the continuous oil phase containing multiple dsGUV encapsulating aqueous medium. The remainder of the frame is filled with a continuous aqueous phase containing a single released GUV. (A-D) The insets display a line profile intersecting the released GUV along the indicated white line for the respective fluorophore. (A) In the oil channel, no traces of remaining oil can be detected on the released GUV. (B) The fluorescent signal of the RhB DOPE is stronger compared to the dsGUV.

This is likely due to reduced diffraction and refraction. (C) and (D) show that no mixing between the aqueous phases was detected.

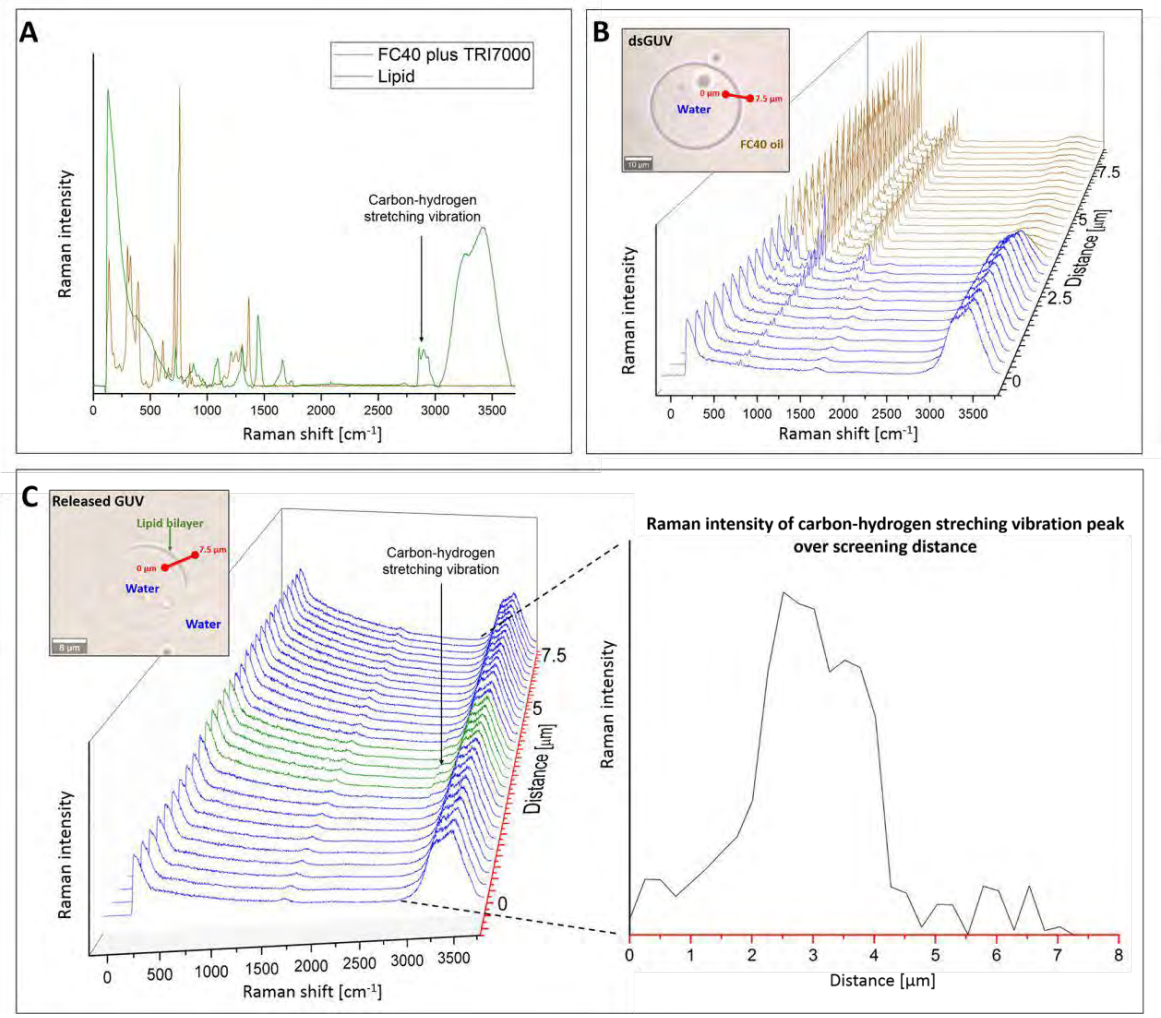

Supplementary Figure 7

Raman spectra of dsGUVs and the released GUVs.

Raman microscope was used to perform Raman spectroscopy on released GUVs to provide a method for the detection of oil/surfactant residues in the released GUVs. (A) Comparison of Raman spectra collected from the solution of surfactants in FC40 oil (brown) and from the SUVs (green), consisting of 4:4:2 of DOPC, POPC and cholesterol, respectively. Carbon-hydrogen stretching vibration of lipid tails indicated by arrow between 2800 and 3000 cm^{-1}.[18] The obtained FC40 oil spectrum in this study present similar peaks as published before.[19] (B) Representative Raman spectra collected through the water oil interphase of the single dsGUV as indicated by the red line in the insert bright-field image. In sake of clarity of presentation the spectra collected from the oil and water phases were brown and blue colored, respectively. (C) Representative Raman spectra collected through the water-lipid interphase of the released GUV as indicated by the red line in the insert bright-field image. In sake of clarity of presentation the spectra collected from the water phases and the lipid bilayer were blue and green colored, respectively. Importantly, no characteristic peaks of the FC40 oil/surfactant were detected

within the collected spectra. Raman intensity of the carbon-hydrogen stretching vibration of lipid tails (indicated by arrow) was plotted over the screening distance.

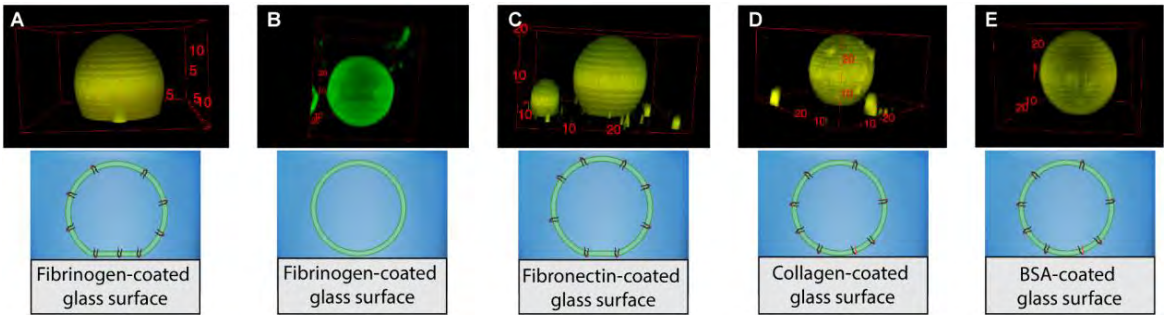

Supplementary Figure 8
Release of integrin-reconstituted GUVs and their functionality assessment.

Representative 3D reconstitution of confocal images of recovered integrin-reconstituted GUVs and their interactions with (A) fibrinogen- (C) fibronectin- (D) collagen- and (E) BSA-coated glass surfaces. The integrin-reconstituted GUVs show strong or moderate adhesion to fibrinogen- or fibronectin-coated glass surfaces, respectively. In comparison, only very weak to no interaction was detected for collagen or BSA-coated surfaces. The merged fluorescence signals consist of ATTO 488-labeled DOPE lipids and TAMRA-labeled $\alpha_{IIb}\beta_3$ integrin. (B) Shows the control experiment in which due to the absence of reconstituted integrin no interaction between the GUV and the fibrinogen-coated glass surface was observed.

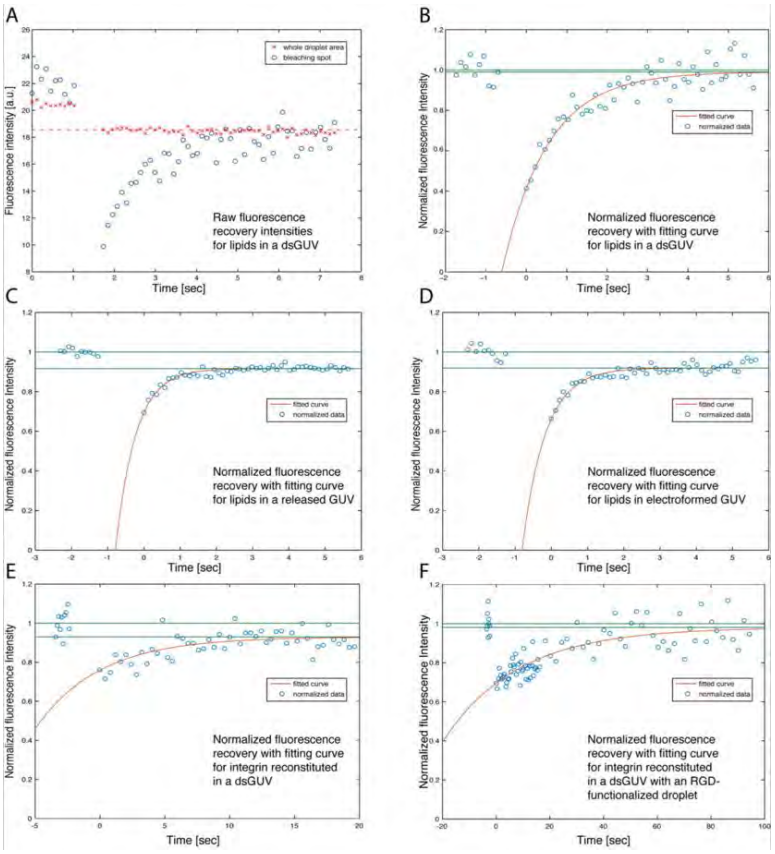

Supplementary Figure 9

Representative recovery curves.

(A) Shows representative raw data acquired for a FRAP measurement on a dsGUV. The data consists of the average intensity values of the bleaching spot and of the whole droplet area in focus. A horizontal dotted line was added as a guide for the eye to indicate photo-fading. Before analysis, all data points were corrected for background. Furthermore, data points were normalized by the average pre-bleaching value and the inverse of the average intensity of the whole droplet in focus was multiplied to the values of the bleaching spot, to correct for photo-fading. The resulting normalized intensity values of the fitting points and fitting curve are presented for the same dsGUV (B). Representative normalized fluorescence recovery curves obtained from the measurements performed on released and produced by electroformation GUVs are presented (C) and (D), respectively. In the FRAP measurements as presented in A-D the same lipid composition containing 0.5 % ATTO 488-labeled DOPE was used as fluorescent marker. (E) and (F) show represented normalized fluorescence recovery curves obtained from the measurements performed on reconstituted TAMRA-labeled integrin proteins in dsGUVs with and without interaction with RGD peptides on the surfactant layer, respectively.

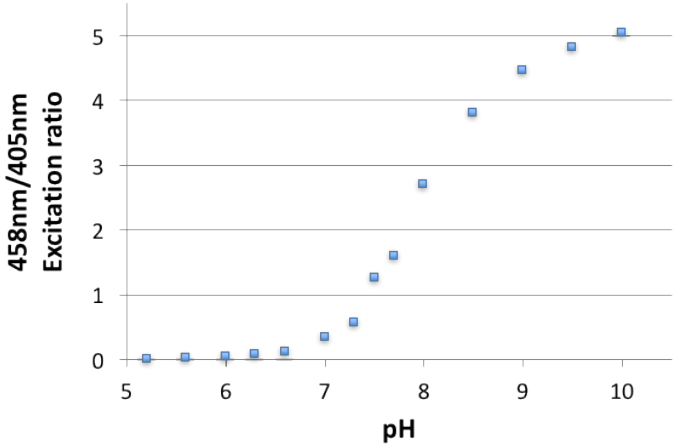

Supplementary Figure 10
Pyranine as a pH sensor within the dsGUVs.

Pyranine was used as a sensor to monitor changes of the dsGUV internal pH. To calibrate the system, dsGUVs were produced with a given pH ranging from 5 to 10 with 1µM pyranine in the aqueous solution. These dsGUVs were then excited at 405 nm and 458 nm wavelength. The figure shows the variation of the fluorescence intensity ratios as a function of a given pH.

Supplementary References

1. Johnson, J.M., Ha, T., Chu, S. & Boxer, S.G. Early Steps of Supported Bilayer Formation Probed by Single Vesicle Fluorescence Assays. *Biophys. J.* **83**, 3371-3379 (2002).
2. Herold, C., Chwastek, G., Schwille, P. & Petrov, E.P. Efficient Electroformation of Supergiant Unilamellar Vesicles Containing Cationic Lipids on ITO-Coated Electrodes. *Langmuir* **28**, 5518-5521 (2012).

3. Platzman, I., Janiesch, J.-W. & Spatz, J.P. Synthesis of Nanostructured and Biofunctionalized Water-in-Oil Droplets as Tools for Homing T Cells. *J. Am. Chem. Soc.* **135**, 3339-3342 (2013).
4. Janiesch, J.W. et al. Key factors for stable retention of fluorophores and labeled biomolecules in droplet-based microfluidics. *Anal Chem* **87**, 2063-2067 (2015).
5. Gu, H., Duits, M.H.G. & Mugele, F. Droplets Formation and Merging in Two-Phase Flow Microfluidics. *International Journal of Molecular Sciences* **12**, 2572-2597 (2011).
6. Xia, Y. & Whitesides, G.M. SOFT LITHOGRAPHY. *Annual Review of Materials Science* **28**, 153-184 (1998).
7. Abate, A.R., Hung, T., Mary, P., Agresti, J.J. & Weitz, D.A. High-throughput injection with microfluidics using picoinjectors. *Proc. Natl. Acad. Sci. U. S. A.* **107**, 19163-19166 (2010).
8. Frohnmayer, J.P. et al. Minimal Synthetic Cells to Study Integrin-Mediated Adhesion. *Angew. Chem.-Int. Edit.* **54**, 12472-12478 (2015).
9. Axelrod, D., Koppel, D.E., Schlessinger, J., Elson, E. & Webb, W.W. MOBILITY MEASUREMENT BY ANALYSIS OF FLUORESCENCE PHOTOBLEACHING RECOVERY KINETICS. *Biophys. J.* **16**, 1055-1069 (1976).
10. Soumpasis, D.M. THEORETICAL-ANALYSIS OF FLUORESCENCE PHOTOBLEACHING RECOVERY EXPERIMENTS. *Biophys. J.* **41**, 95-97 (1983).
11. Gracia, R.S., Bezlyepkina, N., Knorr, R.L., Lipowsky, R. & Dimova, R. Effect of cholesterol on the rigidity of saturated and unsaturated membranes: fluctuation and electrodeformation analysis of giant vesicles. *Soft Matter* **6**, 1472-1482 (2010).
12. Angelova, M.I. & Dimitrov, D.S. Liposome electroformation. *Faraday Discussions of the Chemical Society* **81**, 303-311 (1986).
13. Pott, T., Bouvrais, H. & Meleard, P. Giant unilamellar vesicle formation under physiologically relevant conditions. *Chemistry and Physics of Lipids* **154**, 115-119 (2008).
14. Weinberger, A. et al. Gel-Assisted Formation of Giant Unilamellar Vesicles. *Biophys. J.* **105**, 154-164 (2013).
15. Dimova, R. Recent developments in the field of bending rigidity measurements on membranes. *Adv. Colloid Interface Sci.* **208**, 225-234 (2014).
16. Nagle, J.F. & Tristram-Nagle, S. Structure of lipid bilayers. *Biochim. Biophys. Acta-Rev. Biomembr.* **1469**, 159-195 (2000).
17. Shattil, S.J., Kim, C. & Ginsberg, M.H. The final steps of integrin activation: the end game. *Nat. Rev. Mol. Cell Biol.* **11**, 288-300 (2010).
18. Cherney, D.P., Conboy, J.C. & Harris, J.M. Optical-trapping Raman microscopy detection of single unilamellar lipid vesicles. *Analytical Chemistry* **75**, 6621-6628 (2003).
19. Kim, H.S. et al. Raman spectroscopy compatible PDMS droplet microfluidic culture and analysis platform towards on-chip lipidomics. *Analyst* **142**, 1054-1060 (2017).